7-2014

Baroclinic Transport Time Series of the Antarctic Circumpolar Current Measured in Drake Passage

María Paz Chidichimo

Kathleen A. Donohue
University of Rhode Island, kdonohue@uri.edu

D. Randolph Watts
University of Rhode Island, randywatts@uri.edu

Karen L. Tracey

Citation/Publisher Attribution

Chidichimo, Maria Paz; Donohue, Kathleen A; Watts, D Randolph; Tracey, Karen L. (2014). "Baroclinic Transport Time Series of the Antarctic Circumpolar Current Measured in Drake Passage." Journal of Physical Oceanography. 44(7): 1829-1853.
Available at: http://dx.doi.org/10.1175/JPO-D-13-071.1

Baroclinic Transport Time Series of the Antarctic Circumpolar Current Measured in Drake Passage

Baroclinic Transport Time Series of the Antarctic Circumpolar Current Measured in Drake Passage

MARÍA PAZ CHIDICHIMO,* KATHLEEN A. DONOHUE, D. RANDOLPH WATTS, AND KAREN L. TRACEY

Graduate School of Oceanography, University of Rhode Island, Narragansett, Rhode Island

(Manuscript received 25 March 2013, in final form 5 March 2014)

ABSTRACT

The first multiyear continuous time series of Antarctic Circumpolar Current (ACC) baroclinic transport through Drake Passage measured by moored observations is presented. From 2007 to 2011, 19 current- and pressure-recording inverted echo sounders and 3 current-meter moorings were deployed in Drake Passage to monitor the transport during the cDrake experiment. Full-depth ACC baroclinic transport relative to the bottom has a mean strength of 127.7 ± 1.0 Sverdrups (Sv; 1 Sv ≡ $10^6\,m^3\,s^{-1}$) with a standard deviation of 8.1 Sv. Mean annual baroclinic transport is remarkably steady. About 65% of the baroclinic transport variance is associated with time periods shorter than 60 days with peaks at 20 and 55 days. Nearly 28% of apparent energy in the spectrum computed from transport subsampled at the 10-day repeat cycle of the Jason altimeter results from aliasing of high-frequency signals. Approximately 80% of the total baroclinic transport is carried by the Subantarctic Front and the Polar Front. Partitioning the baroclinic transport among neutral density γ^n layers gives 39.2 Sv for Subantarctic Surface Water and Antarctic Intermediate Water ($\gamma^n < 27.5\,kg\,m^{-3}$), 57.5 Sv for Upper Circumpolar Deep Water ($27.5 < \gamma^n < 28.0\,kg\,m^{-3}$), 27.7 Sv for Lower Circumpolar Deep Water ($28.0 < \gamma^n < 28.2\,kg\,m^{-3}$), and 3.3 Sv for Antarctic Bottom Water ($\gamma^n > 28.2\,kg\,m^{-3}$). The transport standard deviation in these layers decreases with depth (4.0, 3.1, 2.1, and 1.1 Sv, respectively). The transport associated with each of these water masses is statistically steady. The ACC baroclinic transport exhibits considerable variability and is a major contributor to total ACC transport variability.

1. Introduction

The Antarctic Circumpolar Current (ACC) is a major current of the world's oceans. Because it connects the Atlantic, the Pacific, and the Indian Oceans in the Southern Hemisphere, the ACC plays a crucial role in the transfer of mass, heat, freshwater, and other properties among the three ocean basins. ACC transport variability is a key component for the climate system due to its role in the global-scale ocean circulation (Rintoul et al. 2010), and it is therefore an essential feature for modeling efforts to represent accurately. To date, however, the observations to quantify the ACC transport are sparse.

The International Southern Ocean Studies (ISOS) program took place between 1974 and 1981, providing valuable insights on the vertical and horizontal structure of the ACC in Drake Passage. Their measurements consisted of year-long mooring deployments of current-meter moorings and pressure gauges across the passage together with hydrographic sections. The ACC flow was observed to be coincident with three narrow vertically coherent geostrophic jets with large eastward velocities associated with deep-reaching fronts (Nowlin et al. 1977). These fronts are, from north to south, the Subantarctic Front (SAF), Polar Front (PF), and Southern ACC Front (SACCF) (Orsi et al. 1995). More recently, from high-resolution hydrographic sections and maps of the gradient of sea surface height (SSH), a more complex structure of the ACC fronts than earlier coarser sampling suggested was found, with multiple filaments associated with each front merging and diverging along the circumpolar path (Sokolov and Rintoul 2007). In Drake Passage, as many as seven or eight frontal branches were observed at any one time (Sokolov and Rintoul 2009b).

* Current affiliation: National Scientific and Technical Research Council (CONICET), Argentina.

Corresponding author address: María Paz Chidichimo, CONICET/Departamento de Oceanografía, Servicio de Hidrografía Naval, Av. Montes de Oca 2124, C1270ABV, Buenos Aires, Argentina.
E-mail: mpchidichimo@hidro.gov.ar

DOI: 10.1175/JPO-D-13-071.1

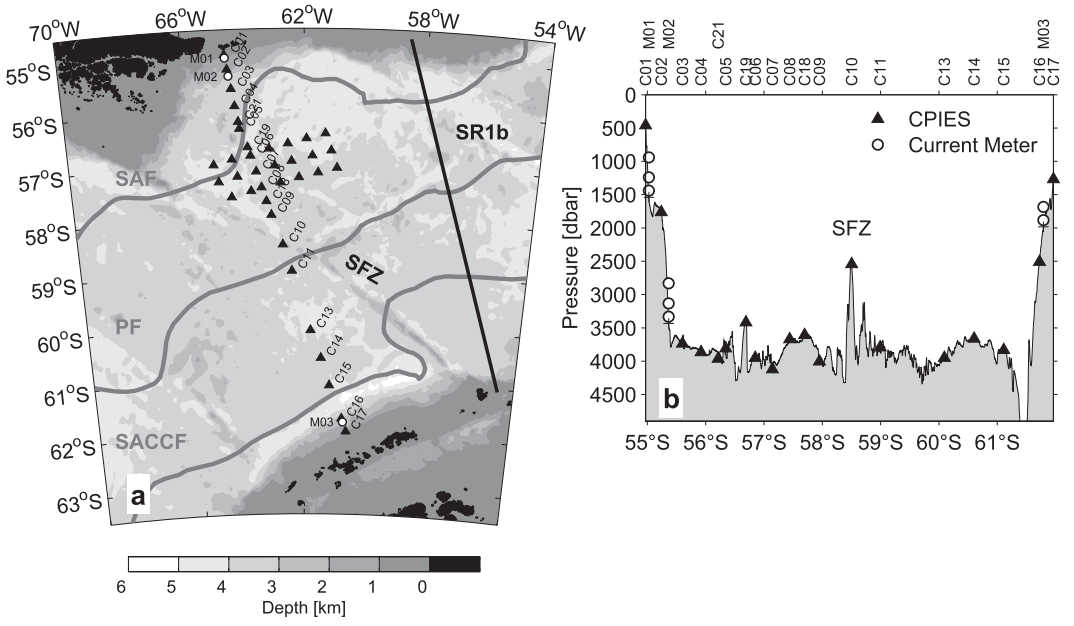

FIG. 1. (a) cDrake transport line and local dynamics array of CPIES (black triangles) and current-meter moorings (white circles). CPIES sites names on the transport line are displayed. Also shown is the WOCE SR1b repeat hydrographic line (black line). The mean positions of the ACC fronts from Orsi et al. (1995) are shown as thick gray lines. The slanting ridge of the SFZ is indicated. Bathymetry comes from Smith and Sandwell (1997). (b) Section of cDrake CPIES (black triangles) and current-meter moorings (white circles) and bathymetry along the transport line.

From the ISOS measurements, Whitworth (1983) and Whitworth and Peterson (1985) estimated the canonical value of the total transport of the ACC of 133.8 Sverdrups (Sv; $1\,\text{Sv} \equiv 10^6\,\text{m}^3\,\text{s}^{-1}$) with a standard deviation of 11.2 Sv for a year-long record. Whitworth and Peterson (1985) constructed a time series of across-passage pressure difference measured at 500-m depth and termed this estimate "barotropic" transport variability. Because total transport was highly correlated to barotropic transport, they concluded that total transport variability on short time scales (seasonal and shorter) is mainly barotropic, implying that ACC transport could therefore be monitored using across-passage bottom pressure differences. Since 1993, the baroclinic component of ACC transport has been monitored from annually repeated hydrographic surveys along the World Ocean Circulation Experiment (WOCE)/Climate Variability and Predictability (CLIVAR) SR1b line between Burwood Bank and Elephant Island (see Fig. 1a). Cunningham et al. (2003) found that the average ACC baroclinic transport relative to zero at the deepest common level was 136.7 Sv with a standard deviation of 7.8 Sv between 1993 and 2000.

Cunningham et al. (2003) revisited the ISOS results in order to interpret the ISOS and hydrographic transports within a consistent baroclinic and barotropic framework. Specifically, baroclinic referred to geostrophic transports relative to the deepest common level. They concluded that there is a significant fraction of the variability (about 35%) in the total transport arising from variations in the baroclinic field. In agreement, a large variability in baroclinic transport was found from upper-ocean XBT measurements (Sprintall 2003) and from numerical models (Olbers and Lettmann 2007). Firing et al. (2011) found from direct velocity observations that the depth-mean and shear components of the transport variability in the upper 1000 m are of similar size.

The difficulty in determining the reference for the ACC and the total transport remains an ongoing issue (Meredith et al. 2011; Firing et al. 2011). Cunningham et al. (2003) found that including lowered acoustic Doppler current profiles (LADCP) data to obtain the total transport along the SR1b sections increased the uncertainty of the transport estimate. Recently, Griesel et al. (2012) combined mean dynamic ocean topography products with climatological ocean density fields. Resulting ACC transports were generally higher than observational estimates. They attribute these discrepancies to a lack of mass conservation in the products as well as the difficulty in resolving the high temporal variability and small spatial scales characteristic of the Southern Ocean.

The Southern Ocean has been shown to be especially susceptible to climate change. In the past three decades a strengthening of the westerly winds in the Southern Ocean has been observed (Thompson and Solomon

2002), thereby resulting in a higher southern annular mode (SAM) index. Aoki (2002) found significant correlations between observations of sea level variations around Antarctica and the SAM on time scales from a few days to several weeks, and Meredith et al. (2004) found significant interannual variability in the circumpolar westerly winds that was correlated to fluctuations in the observed ACC transport. Baroclinic ACC transport estimates have been remarkably steady despite a SAM increase. From the analysis of profiling floats and historical hydrography, Böning et al. (2008) suggested that ACC transport is relatively insensitive to decadal changes in wind stress. To date there is no observational evidence of a long-term increase in transport due to changes in the SAM.

Hydrographic transects are irregular and infrequent, making the analysis of variability or the detection of trends in the ACC transport very difficult. Sampling at high spatial and temporal resolution is necessary to avoid significant aliasing of high-frequency variability. Meredith and Hughes (2005) concluded that sampling with an interval shorter than a week was required to reliably monitor interannual changes in the ACC, and more rapid sampling is required to resolve subseasonal and seasonal variations.

The cDrake array was deployed in November–December 2007 in Drake Passage providing unprecedented temporal and spatial resolution to resolve the subseasonal-to-interannual variability and dynamics of the total ACC transport over a period of 4 yr (Fig. 1; Chereskin et al. 2009, 2012). The array consists of 37 inverted echo sounders (IESs) equipped with bottom pressure gauges and current meters [current- and pressure-recording IESs (CPIES)] and 2 current-meter moorings on the northern continental slope and 1 on the southern continental slope. Among the specific goals of the cDrake array are to determine the time-varying total ACC transport, its vertical structure partitioned between baroclinic and barotropic components, and its lateral partitioning among the jets that compose the ACC.

The purpose of this study is to describe the mean, variability, and partitioning of the baroclinic component. The cDrake array provides an excellent opportunity to determine the unaliased mean full-depth baroclinic transport and also to explore the time scales of the observed fluctuations using the 4-yr dataset from December 2007 through October 2011. Here, we adopt the Cunningham et al. (2003) definition of baroclinic transport. This allows straightforward comparisons to previous ACC transport estimates using hydrography. This paper is structured as follows. In section 2, we introduce the data used in this study. Section 3 establishes the methodology to determine the baroclinic transport and discusses the associated error estimates. Section 4 details the mean and temporal variability of the observed baroclinic flow, the lateral partitioning of the baroclinic transport among fronts, and the vertical distribution of baroclinic transport among neutral density layers. Section 5 compares our baroclinic transport estimate with previous studies. Section 6 provides the discussion and summary.

2. Data

a. cDrake experiment overview

The cDrake array was deployed in November–December 2007 to monitor the ACC transport in Drake Passage and operated continuously until late 2011. The array consists of a transport line spanning 800 km across Drake Passage and a local dynamics array located where surface variability is at a maximum between the SAF and PF (Fig. 1a). The mean positions of the SAF, PF, and SACCF are nominally at 56°, 58.5°, and 60.75°S, respectively (Orsi et al. 1995). Four prominent bathymetric features across Drake Passage are the steep northern continental slope, the Shackleton Fracture Zone (SFZ) that slants across our array near 58.5°S, the South Shetland Trench near 61.5°S, and the southern continental slope (Figs. 1a,b).

Throughout this study, we describe and analyze data from the transport line (sites labeled in Fig. 1a). The nominal positions, water depths, and periods of the records of the CPIES located in the transport line and the current-meter moorings are given in Tables 1 and 2, respectively. The CPIES in the transport line span from the 500-m isobath in the north to the 1200-m isobath in the south (Figs. 1a,b). Two deep current-meter moorings are located on the northern slope and one on the southern slope (Figs. 1a,b). The spatial resolution between CPIES sites ranges between 45 and 65 km, with higher spatial resolution north of 57.5°S and within the SAF and near topography. The CPIES measures bottom pressure, round-trip acoustic travel time to the sea surface and back τ, and currents 50 m above the bottom using an Aanderaa Doppler current sensor. On the northern slope each of the two moorings carries three current meters at 100, 300, and 600 m above the bottom. On the southern slope, the mooring carries two current meters at 100 and 300 m above the bottom (Fig. 1b; Table 2). The three current-meter moorings aim to directly observe for 2 yr the vertical structure of the flow and to resolve bottom trapping along the northern and southern continental slopes. After deployment in 2007, yearly telemetry cruises were carried out in 2008, 2009, and 2010, and CPIES instruments were replaced as needed. Recovery of all the instruments took place in December 2011.

Overall, data return was very good with only a few data losses. C01 was located at the steep continental

TABLE 1. Nominal position, water pressure, and dates of CPIES distributed across the transport line in Drake Passage from north to south.

CPIES name	Lat (S)	Lon (W)	Water pressure (dbar)	Dates
C01	54°58.1′	64°35.5′	476	15 Nov 2007–21 Nov 2011
C02	55°14.2′	64°31.1′	1783	15 Nov 2007–17 Nov 2008 and 17 Dec 2009–21 Nov 2011
C03	55°36.0′	64°24.2′	3662	15 Nov 2007–21 Nov 2011
C04	55°55.2′	64°18.2′	3866	15 Nov 2007–21 Nov 2011
C21	56°12.8′	64°12.0′	3890	12 Dec 2008–21 Nov 2011
C05*	56°20.6′	64°10.1′	3829	15 Nov 2007–5 Dec 2008
C19	56°41.5′	63°54.7′	3445	15 Nov 2007–21 Nov 2011
C06	56°50.9′	63°49.3′	3928	15 Nov 2007–21 Nov 2011
C07	57°08.7′	63°38.1′	4136	15 Nov 2007–21 Nov 2011
C08	57°26.4′	63°28.0′	3684	15 Nov 2007–21 Nov 2011
C18	57°41.8′	63°18.3′	3608	15 Nov 2007–5 Dec 2008
C09**	57°57.0′	63°08.6′	4000	15 Nov 2007–21 Nov 2011
C10	58°30.1′	62°45.2′	2502	15 Nov 2007–21 Nov 2011
C11	58°59.0′	62°26.0′	3840	15 Nov 2007–21 Nov 2011
C13	60°05.5′	61°45.9′	3956	15 Nov 2007–21 Nov 2011
C14	60°36.2′	61°22.4′	3667	15 Nov 2007–21 Nov 2011
C15	61°06.7′	61°02.8′	3836	15 Nov 2007–17 Oct 2011
C16	61°43.4′	60°32.9′	2508	15 Nov 2007–21 Nov 2011
C17	61°57.7′	60°22.5′	1267	15 Nov 2007–21 Nov 2011

* Recovered in December 2008 due to current-meter failure.
** Noisy τ record during first deployment year.

slope north of the passage in shallow water. Strong currents dragged the instrument to different depths episodically throughout the deployment, introducing numerous changes in both the pressure and τ records that were difficult to identify and remove. Therefore, data from C01 have been excluded from the transport analysis. Close to the northern slope, C02 was recovered in November 2008 due to current-meter failure, and subsequently the site was reoccupied with a new CPIES. In austral spring 2009 it was not possible to establish communication with the CPIES leaving a data gap of 1 yr at C02 (from 18 November 2008 to 16 December 2009; Table 1). C02 was redeployed and worked without problems until recovery in November 2011. As described in section 2d, this gap was filled by using the data from the northernmost current-meter mooring. C05 was recovered in austral spring 2008 due to current-meter failure, and abrupt increases in pressure were found in the records, indicating that the instrument slid down the steep topography. Therefore, for subsequent years the site was relocated to flatter topography and termed C21. The nearby records at C05 and C21 are merged together to obtain a 4-yr-long time series at the nominal C05 site. C09 measured noisy τ data during the first deployment year; thus, it was recovered in austral spring 2008 and replaced. The noisy τ record was replaced with data from the neighboring C18 site. All moored current meters worked well except the uppermost current meter at M02, which failed a few months after deployment (but has a complete temperature record) and the bottommost current meter and temperature sensor at M02, which failed immediately after deployment (Table 2).

b. *Data acquisition and processing*

A detailed description of the data processing can be found in Tracey et al. (2013). Here we will describe briefly how the measured τ, pressure, and currents are processed. The IES measures the τ of a 12.0-kHz pulse

TABLE 2. Position, nominal current-meter pressures, water pressure, and dates of current-meter moorings at the northern and southern slopes of the section.

Name	Lat (S)	Lon (W)	Nominal current-meter pressures (dbar)	Water pressure (dbar)	Dates
M01	55°01.6′	64°34.5′	920, 1220, 1420	1520	16 Nov 2007–20 Nov 2009
M02	55°21.9′	64°28.7′	2755,* 3055, 3255**	3355	16 Nov 2007–21 Nov 2009
M03	61°47.4′	60°30.1′	1684, 1884	1984	23 Nov 2007–30 Nov 2009

* Current meter failed a few months after deployment.
** Current meter and temperature sensor failed immediately after deployment.

from the sea bottom to the surface and back. Within every hour, the CPIES transmits 24 pings, and subsequently they are processed using a two-stage windowing and median filtering in order to reduce scatter due to sea surface roughness, yielding an hourly estimate. The bottom pressure values are averaged to obtain hourly estimates. Subsequently, the pressures are dedrifted and leveled to a common geopotential following Donohue et al. (2010), and tidal response analysis is performed to remove the semidiurnal and diurnal tides (Munk and Cartwright 1966). Two corrections are applied to the currents: rotation to true north accounting for local magnetic declination and a sound speed correction appropriate for each instrument's depth. The hourly time series of all variables are 72-h low-pass filtered using a fourth-order Butterworth filter, and 24 h at the beginning and end of the records are truncated to avoid transients. Last, all variables are subsampled to yield 12-hourly estimates. Throughout this paper the filtered 12-hourly estimates of τ will be used, except for the aliasing calculation (section 4c) where we use the hourly records of τ and construct a baroclinic transport time series to examine the high-frequency variance of geopotential height.

c. *Gravest empirical mode*

The gravest empirical mode (GEM) (Meinen and Watts 2000) is a lookup table created from hydrography in the region. The table relates τ integrated between the surface and a selected reference depth τ_{index} to hydrographic profiles of temperature T, salinity S, and specific volume anomaly δ. In the ACC region, where pronounced meridional gradients and associated strong baroclinicity exist, the GEM technique has been successfully utilized (Sun and Watts 2001; Swart et al. 2010; Behnisch et al. 2013). South of Australia, the GEM fields captured more than 97% of the density and T variance (Sun and Watts 2001). Furthermore, Watts et al. (2001) found very good agreement between estimates of T and S from IES measurements through the GEM relation with directly measured T and velocity from current-meter moorings south of Australia in the ACC. For full details on how a GEM is constructed, the reader is referred to Donohue et al. (2010).

For the cDrake experiment, the construction of the GEM is discussed in Cutting (2010) and Firing et al. (2014). Here, we briefly review important aspects and the appendix provides additional details. A reference depth of 2000 dbar is chosen, as a compromise between having a large number of casts to construct the GEM by including Argo profiles and requiring the τ_{index} to capture the gravest mode variability of the water column. The cDrake GEM is based on 526 hydrographic profiles coming from Argo floats, cDrake calibration CTDs, and historical hydrography in the region with the condition that all selected casts extended to 2000 dbar or greater (Cutting 2010). The latitudinal extent of the region was chosen between 54.5° and 64.5°S and was determined by the landmasses, while the longitudinal extent of the region spans between 57° and 80°W and was chosen based on the range of τ values corresponding to the casts on those regions. The profiles cover the time period 1972–2011. Recently, Meijers et al. (2011a,b) constructed a "satGEM." Satellite altimeter SSH was used as a proxy for geopotential height. Profiles of T and S were determined as a function of time and space using a time-invariant GEM. Differences between satGEM and hydrography are then interpreted as either "adiabatic" (e.g., due to a shift of circumpolar fronts) or "diabatic" (e.g., due to changes in water masses). In the cDrake GEM, the bulk of the casts are from the last decade, and most of the deep-reaching casts were acquired during the cDrake cruises. Thus, our GEM is time invariant, and any secular or interannual water mass variability contributes to the scatter.

To remove errors associated primarily with upper-ocean seasonal variability, the seasonal signals are removed from the GEM and τ records following Watts et al. (2001) and Cutting (2010). The GEM is created by fitting a spline curve to these deseasoned data as a function of τ_{index} at a suite of pressure levels. To guide the appropriate amount of smoothing to perform, a priori errors (Bindoff and Wunsch 1992; Sun and Watts 2001) were estimated for each level from the hydrocasts and compared to the GEM rmse profiles. Subsequently the fitted curves were interpolated to a 10-dbar spacing spanning from the surface to 4500 dbar.

At the southernmost site (C17; Fig. 1), the GEM calculated using a 2000-dbar reference level does not account for the large τ values due to the cold temperatures in the Antarctic continental slope. Therefore, another GEM is constructed to be used at the C17 site with τ_{index} integrated between the surface and 1000 dbar. The same method as described above is employed by including additional CTD casts to 1000–1500 dbar close to the coast at the southern end of Drake Passage.

GEM quality is expressed as how much of the signal variance is captured by the GEM (e.g., Meinen and Watts 2000; Sun and Watts 2001). Both the T and δ GEMs explain over 93% of the variance in the upper 2500 dbar and for S in the 500–1500-dbar range, below which the accuracy of the GEM remains high and the S signal is relatively weak. The geopotential anomaly GEM explains 98% and 70% at the surface and 3800 dbar, respectively. These are illustrated in Fig. A4 in the appendix. Firing et al. (2014) compared cDrake CPIES-determined

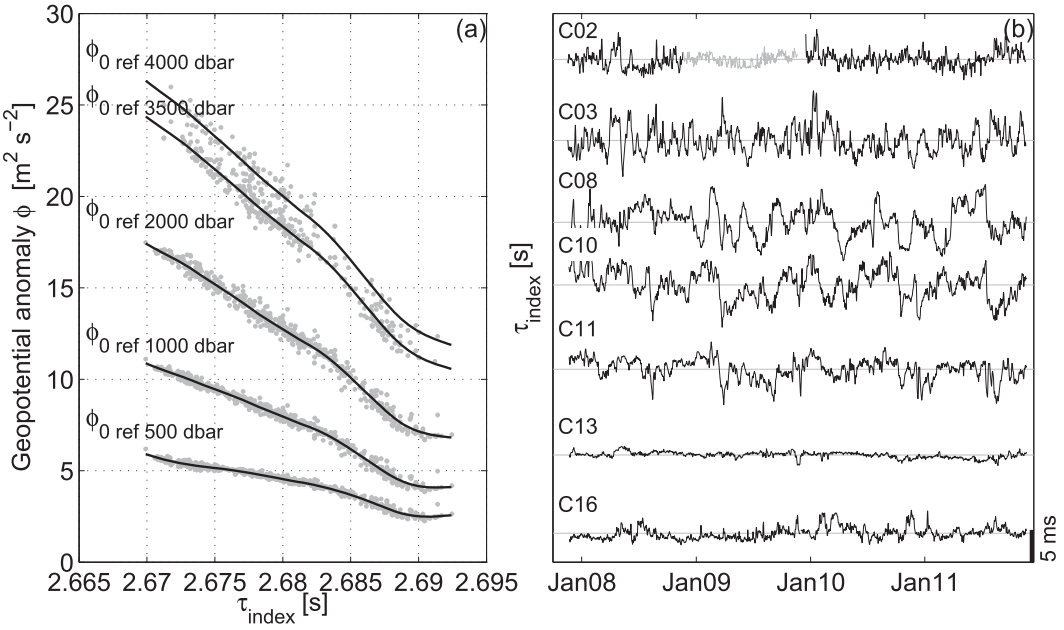

FIG. 2. (a) Geopotential anomaly ϕ at the surface relative to five pressure levels as a function of round-trip travel time between the surface and 2000 dbar (i.e., τ_{index}) from the individual CTDs (gray dots) together with ϕ at the surface relative to these five pressure levels from the GEM lookup table (black lines). (b) Time series of τ_{index} at representative sites across Drake Passage. The gray line at C02 is the τ_{index} record estimated using M01 current-meter data (see section 2d).

temperatures to a nearby mooring (termed M4) deployed during the Drake experiment (Ferrari et al. 2012) in northern Drake Passage. Firing et al. (2014) found excellent agreement: rms differences (correlations; r^2) are 0.25°C (0.85) at 520 dbar, 0.09°C (0.90) at 930 dbar, and 0.07°C (0.86) at 2540 dbar. At 520 dbar, where the rms difference is largest, M4 temperature has a standard deviation of 0.47°C, indicating that the rms difference is about half the signal standard deviation. Additional analyses of these records (not shown) reveals that the coherence-squared estimates between the records are high (>0.85) for frequencies lower than 1/10 day^{-1} and decrease to about 0.6 for higher frequencies, indicating that most of the GEM scatter arises from high-frequency variability.

Moreover, Fig. 2a shows a robust relationship between τ_{index} and the geopotential anomaly ϕ throughout the water column. The rms difference between ϕ from the individual CTDs versus ϕ from the GEM lookup table integrated between the surface and 500, 1000, 2000, 3500, and 4000 dbar is 0.11, 0.18, 0.31, 0.44, and 0.52 m^2 s^{-2} rms, respectively. As expected, the scatter increases when integrating over larger depths.

d. *Acoustic travel time τ measurements*

To interpret CPIES-measured τ utilizing the GEM table, τ values are converted to τ_{index} as described in Tracey et al. (2013). Time series of τ_{index} at representative sites across the passage are shown in Fig. 2b. The large, lower-frequency τ fluctuations are observed at sites located under the meandering SAF and PF (such as C03, C08, C10, and C11). CPIES located on the continental slopes, such as C02 and C16, exhibit variability with higher frequency. The records at sites occupied in the southern portion of the Drake Passage poleward of the PF (like C13) exhibit considerably weaker variability. The gap during the second year at C02 is filled by using the M01 current-meter data (Table 2) to create a "pseudo-IES" travel time τ_{cm}. Following Meinen and Watts (2000), the temperature lookup table $T_{\text{GEM}}(p, \tau)$ is inverted to obtain $\tau(p_{\text{cm}}, T_{\text{cm}})$, where T_{cm} is the temperature measured by current meters at three levels. Pressure p_{cm} was measured only at the top level, so that record was offset by the mooring line lengths to provide estimates of p_{cm} at the two deeper levels. A single τ_{cm} record is created by averaging the three estimates. The τ_{cm} appears to underestimate the variability at C02 located farther offshore (gray line in Fig. 2b).

The error estimates closely follow the steps outlined in Baker-Yeboah et al. (2009) and Donohue et al. (2010). There are four independent sources of error for 72-h low-pass-filtered τ: (i) the scatter in τ due to sea surface roughness of 0.07 ms; (ii) the conversion to a purely steric τ by removal of pressure-associated

pathlength change has an error of 0.02 ms (mostly associated with uncertainty on the pressure drift); (iii) the error associated with the conversion from measured τ to a dynamic τ independent of a latitudinal dependence of gravity of 0.03 ms; and (iv) the conversion of the dynamic τ (typically for 3500–4200-dbar depth) to τ_{index} (for 2000-dbar index pressure) of 0.15 ms. Thus, the total error in τ_{index} results from summing the independent errors in a square root of the sum of squares sense and amounts to 0.17 ms [$\delta\tau = \sqrt{(0.07)^2 + (0.02)^2 + (0.03)^2 + (0.15)^2} = 0.17$ ms]. To obtain the error for the unfiltered hourly record of τ, we substitute for (i) the scatter of 0.45 ms associated with typical scatter of 24 pings in an hour of 1.7–2.5 ms (using a midrange value of 2.2 ms gives $2.2/\sqrt{24} = 0.45$ ms). Substituting this number in $\delta\tau$, we get an error of 0.48 ms for hourly τ. The pseudo-IES τ_{cm} has an estimated accuracy of 4.6 ms (bias of 4.5 ms from the current-meter pressure and temperature measurement errors and scatter of 0.9 ms from the inverted lookup table). This error estimate is improved by excluding the bias. Because M01 and C02 were not collocated, an offset in their mean τ is expected regardless of the bias error, so the bias is eliminated by forcing the means at M01 and C02 during the first year to agree. Thus, the accuracy of τ_{cm} is 0.9 ms. This is consistent with the standard deviation of the difference between M01 τ_{cm} and C02 τ of 1.2 ms determined for the period when the records overlapped.

3. Baroclinic transport calculation

a. Methods

This section describes how the baroclinic transport time series through the passage is computed using the τ records at each site in the transport line (Figs. 1a,b; Table 1). There is a robust relationship between vertical profiles of T, S, δ, and therefore of geopotential height anomaly $\phi(p)$ and the measured τ, expressed in the GEM lookup table (Fig. 2a and the appendix). Using $\phi(p)$ between selected pressure levels p and a reference pressure $p_{\text{ref}}[\phi(p) = \int_{p_{\text{ref}}}^{p} \delta(p')\,dp']$ at two laterally separated sites, geostrophy allows us to compute vertical profiles of the normal component of the baroclinic velocity $u_g(p)$ at a pressure p relative to p_{ref} between two sites 1 and 2:

$$u_g(p) = \frac{\phi_1(p) - \phi_2(p)}{fL}, \tag{1}$$

where f is the Coriolis parameter and $L = x_1 - x_2$, where x_1 and x_2 represent the locations of the sites.

The geostrophic baroclinic transport at each time step is then computed as the vertical and lateral integral of the geostrophic velocities $u_g(p)$ from the surface to a reference depth level over horizontal separation between sites. To facilitate comparison with previous estimates from hydrography, the baroclinic transport is computed relative to the bottom.

To obtain the full across-passage baroclinic flow, we compute transports in three regions and subsequently we sum them: 1) the northern slope inshore of the 3500-m isobath between C01 and C03, 2) the middle of the section between C03 and C16, and 3) the southern slope inshore of the 2500-m isobath between C16 and C17 (Fig. 1b). The reported variability of the 4-yr time series in each region represents one standard deviation from the mean.

The northern slope transport is estimated as follows. Between C01 and C02, we only estimate the mean velocity structure to capture the mean transport contribution because the C01 time series failed (section 2a). First, between the surface and 400 m, we estimate the velocity shear relative to 400 m [deepest common level (DCL) between C01 and C02] from CTD data from each of the five cDrake cruises, and subsequently the five shear profiles are averaged together. Next, between 400 and 927 m (mean measured upper M01 current-meter depth), the mean velocity shear of 11 cm s^{-1} is determined by averaging 40 LADCP casts taken near C02 on the cDrake cruises. Then, the 400–927-m shear is added to the mean upper M01 current-meter velocity rotated in the direction of the northern transport line (Table 2) of 8 cm s^{-1}, resulting in 19 cm s^{-1}. A mean profile from the surface to 927 m is created by referencing the mean CTD-derived shear profile by this amount. Next, the mean absolute velocity profile between 927 m and the bottom at 1427 m is determined by the deep mean velocities from the three current meters at the M01 mooring rotated in the direction of the northern transport line (Table 2). Subsequently, a mean absolute velocity profile from the surface to 1427-m depth with 2-dbar spacing is created by linear interpolation. Finally, to be consistent with our barotropic convention, the mean absolute velocity profile is referenced to zero at 1427-m depth. Integrating this mean velocity profile over a distance of 29 km between C01 and C02 and through 1427-m depth gives 4.8 Sv, with an error of 3.3 Sv. The accuracy of the mean transport of 3.3 Sv is calculated as $\sqrt{\sigma_{\text{CTD}}^2 + \sigma_{\text{LADCP}}^2 + \sigma_{\text{cm}}^2}$, where $\sigma_{\text{CTD}} = 0.9$ Sv, $\sigma_{\text{LADCP}} = 1.6$ Sv, and $\sigma_{\text{cm}} = 2.7$ Sv are the transport standard deviations obtained for the CTDs, LADCPs, and current meters, respectively.

Then, we estimate the transport between C02 and C03 using Eq. (1). There is additional transport in the bottom triangle of the water column below the depth of the

shallower of any neighboring pair of $\phi(p)$ profiles. To account for this transport and its error between C02 and C03, we use the following method. At each time step, we linearly interpolate τ on a 2-km lateral grid between C02 and C03. At each interpolated τ, we look up $\phi(p)$ and evaluate the transport geostrophically for each subsection relative to and above 3500 m (approximate depth at C03) considering two referencing possibilities: (i) for each 2-km-wide subsection, we assume zero velocity below topography, which gives a transport of 15.1 ± 11.6 Sv; and (ii) for each 2-km-wide subsection, we assume zero velocity at the DCL above topography, which gives a transport of 13.4 ± 10.4 Sv. Finally, (iii) we estimate the baroclinic transport between C02 and C03 relative to 3500 m, which gives a transport of 16.1 ± 12.1 Sv. This close agreement indicates that our transport estimate relative to 3500 m is a good representation of the transport through the section between C02 and C03. The error due to possible additional transport in unresolved bottom triangles is given by the range of estimates of the mean baroclinic transport using the three different methodologies (i), (ii), and (iii) and amounts to 16.1 − 13.4 = 2.7 Sv between C02 and C03. The total transport along the northern slope, from C01 to C03, becomes 20.9 ± 12.1 Sv.

For the central deep passage (between C03 and C16), we compute the baroclinic velocity relative to the deepest level between each station pair across the passage using Eq. (1), and subsequently, we sum vertically and across the passage. The transport in this 716 km wide by approximately 4000-m-deep region is 105.4 ± 14.7 Sv. To obtain bottom triangle error estimates across the topography at the SFZ (from C09 to C11), between C11 and C13, and close to the South Shetland Trench, the analyses are analogous to those described at the northern boundary. Applying the three methodologies produced a range in the mean baroclinic transport of 2.8 Sv between C09 and C11, 0.5 Sv between C11 and C13, and 0.6 Sv between C15 and C16. For the latter, the method mostly considers the sloping bathymetry near C16. Note in passing that there was a CPIES (termed C12) deployed between C11 and C13 during only the first 2 yr of cDrake. Estimating the transport between C11 and C13 during those 2 yr including C12 produced no change in the mean transport compared with the estimate excluding C12 (not shown).

On the southern slope, we evaluate the baroclinic transport relative to and above 1260 m between C16 and C17, which gives a mean transport of 1.4 ± 1.7 Sv. The mean velocities from the current meters at M03 rotated in the direction of the southern transport line (Table 2) are small: 0.9 cm s^{-1} at ~1709 m and −0.7 cm s^{-1} at ~1909 m. They indicate a zero crossing close to ~1800 m. Alternatively, if the velocity shears are extrapolated to zero velocity at 1800 m, a mean transport of 1.5 ± 1.8 Sv results. The small increase indicates that the deep shear does not significantly alter the transport at the southern slope. We choose to use the transport estimate referenced to zero at 1260 m.

TABLE 3. Baroclinic transport error estimates (Sv) for the transport time series discussed in section 4. The bottom triangle transport error (section 3a) for each transport time series is given in column 2. The total error for each transport time series combining the bottom triangle error and the uncertainty in the estimate of geopotential anomaly ϕ for 72-h and >10-day low-pass-filtered data are given in columns 3 and 4, respectively. The total error calculation is detailed in section 3b.

	Bottom triangle	72-h low pass	>10-day low pass
Northern slope	2.7	6.9	3.7
Central deep passage	2.9	8.9	4.3
Southern slope	—	3.8	1.5
Total baroclinic	4.0	11.9	5.9
SAF/PF	3.9	9.3	5.1
SACCF	0.6	8.4	3.3
SASW/AAIW	—	3.2	1.1
UCDW	—	5.8	2.0
LCDW	3.9	8.3	4.7
AABW	0.8	1.0	0.8

Layer transports based on neutral density (γ^n; Jackett and McDougall 1997) surfaces as the limits are also calculated. The water masses in the ACC can be approximately separated by the following γ^n layers (e.g., Speer et al. 2000; Naveira Garabato et al. 2003): Subantarctic Surface Water (SASW) and Antarctic Intermediate Water (AAIW) lighter than 27.5 kg m^{-3}; Upper Circumpolar Deep Water (UCDW) 27.5–28.0 kg m^{-3}; Lower Circumpolar Deep Water (LCDW) 28.0–28.2 kg m^{-3}; and Antarctic Bottom Water (AABW) denser than 28.2 kg m^{-3}. For this analysis, layer depths are calculated at each time step by evaluating the γ^n structure across the cDrake section looking up T and S from the GEM tables.

b. Error analysis

Transport uncertainty arises from two sources: the accuracy of the estimate of $\phi(p)$ and the error due to additional transport in the bottom triangle of the water column below the depth of the shallower of any neighboring pair of $\phi(p)$ profiles. Table 3 provides error estimates for the transports discussed in section 4.

Here, we detail the methodology as applied to the central deep passage (between C03 and C16). The ϕ uncertainty has contributions from GEM and τ_{index} uncertainty and decreases with low-pass filtering separately as follows. As discussed in section 2c, part of the

GEM scatter is due to high-frequency variability. Using the coherence estimates between M4-measured and CPIES-derived temperature as a guide, we classify errors for a 72-h low-pass-filtered ϕ and a >10-day low-pass-filtered ϕ. The rms scatter about the fit between ϕ at the surface relative to 4000 m and τ_{index} is $\delta\phi = 0.52\,\text{m}^2\,\text{s}^{-2}$; the standard error of the fitted curve is $\delta\phi = 0.17\,\text{m}^2\,\text{s}^{-2}$ (Fig. 2a). For the 72-h low-pass-filtered data, the former is used; for the >10-day low-pass-filtered data, the latter is used.

The accuracy of the CPIES-measured τ_{index} is $\delta\tau = 0.17$ ms (section 2d). Detailing the calculation for the 72-h low-pass-filtered data, the combined ϕ error is $\Delta\phi = \sqrt{[(\partial\phi/\partial\tau)\delta\tau]^2 + (\delta\phi)^2} = 0.53\,\text{m}^2\,\text{s}^{-2}$. Assuming that the errors in the two ϕ estimates on either side of Drake Passage are independent, and substituting $\Delta\phi$ in $\Delta u_g = (\sqrt{2}\Delta\phi)/(fL)$, along with $L = 716$ km and a Coriolis parameter f of $1.2 \times 10^{-4}\,\text{s}^{-1}$, gives $0.87\,\text{cm}\,\text{s}^{-1}$. The temporal average of the velocity shears between C03 and C16 indicates that the mean surface velocity is about 3 times the depth-averaged mean velocity profile (not shown). Assuming the velocity error decreases in a manner similar to the mean shear structure, the depth-averaged velocity error is $0.29\,\text{cm}\,\text{s}^{-1}$ [$(1/3) \times 0.87$]. The accuracy in the 72-h low-pass-filtered baroclinic transport from the accuracy of ϕ is 8.4 Sv. The uncertainty associated with the sloping bathymetry near the SFZ, between C11 and C13, and between C15 and C16 is 2.8, 0.5, and 0.6 Sv, respectively (section 3a). The bottom triangle error amounts to $\sqrt{(2.8)^2 + (0.5)^2 + (0.6)^2} = 2.9$ Sv. The total error for the central deep passage transport is obtained by combining either the 72-h or >10-day low-pass-filtered values from the uncertainty in ϕ with the bottom triangle estimates. The total error for the central deep passage 72-h low-pass-filtered baroclinic transport becomes $\sqrt{(8.4)^2 + (2.9)^2} = 8.9$ Sv. Carrying out this calculation for the >10-day low-pass-filtered estimates results in an error of 4.3 Sv. These calculations are repeated for the northern and southern slope regions. Errors for all three regions are listed in Table 3. The error for the baroclinic transport across the full Drake Passage is obtained by combining the errors from the three regions. We obtain error estimates for the total baroclinic transport of 11.9 and 5.9 Sv, for 72-h and >10-day low-pass-filtered records, respectively.

For the layer transports, there will be an additional source of baroclinic transport error arising from the uncertainty in determining layer thickness h. For each γ^n surface we examine the difference between the γ^n surface depth determined from CTDs and γ^n surface depth determined from the GEM T and S using each CTD's τ_{index}. This scatter provides an estimate of layer depth uncertainty Δh. The ϕ error is estimated from the scatter in the ϕ GEM relative to 4000 dbar integrated in layers between 0 and 500, 500 and 1500, 1500 and 3500, and 3500 and 4000 dbar. For the 72-h low-pass-filtered data, the rms of the h and ϕ scatter are used; for the >10-day low-pass-filtered data, the standard error is used instead. We assume that the ϕ error and the layer depth error are independent. The combined error becomes $L\sqrt{(\Delta u_g h_{\text{mean}})^2 + (u_{g_{\text{mean}}}\Delta h)^2}$, where L, h_{mean}, and $u_{g_{\text{mean}}}$ are the mean width, thickness, and velocity within the layer. There will be an additional contribution from the bottom triangles. These errors are provided in Table 3. The LCDW layer has the largest error due to the contribution of the bottom triangle transport error from the northern slope and the SFZ.

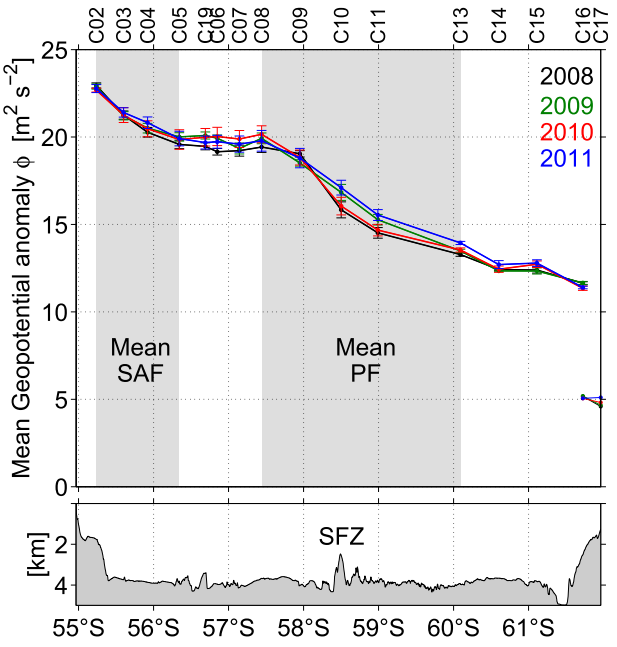

FIG. 3. The 1-yr temporal means of geopotential anomaly ϕ at the sea surface relative to 3500 m at each CPIES site. To confirm interannual consistency also at C17, the mean ϕ at the sea surface relative to 1260 m is shown. To facilitate comparison with C17, at C16 the mean ϕ at the sea surface relative to 1260 m is also shown. Colors indicate each deployment year: 2008 (black), 2009 (green), 2010 (red), and 2011 (blue). Error bars indicate standard error of the mean ϕ. Labels at the top indicate the names of the CPIES sites. The gray shading indicates the mean positions of the SAF and the PF. Bathymetry section is also shown at the bottom. The position of the SFZ is indicated.

4. Results

a. Mean baroclinic structure across Drake Passage

The strikingly steady pattern of the annual-mean baroclinic structure across the passage is illustrated by the mean ϕ at the sea surface relative to 3500 m (except at C17, where we evaluate ϕ at the surface relative to 1260 m) at each CPIES site (Fig. 3). To detect possible

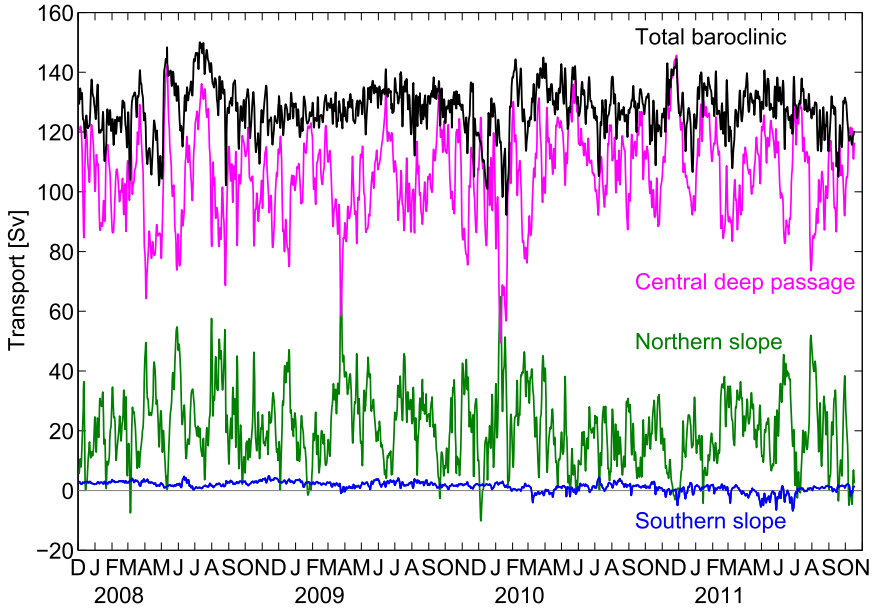

FIG. 4. Time series of the 72-h low-pass-filtered baroclinic transport through Drake Passage vertically integrated from the bottom to the surface (black) and its constituents: baroclinic transport at the northern slope north of the 3500-m isobath (green), in the central deep passage section excluding the slopes (magenta), and at the southern slope south of the 2500-m isobath (blue). Positive transports correspond to eastward flow. For details of the calculation see section 3a.

interannual changes in the baroclinic structure, we evaluate the mean ϕ for four approximately year-long segments defined by cruises and data retrieval. Throughout this paper, the year-long segments are defined from December 2007 to mid-November 2008, from mid-November 2008 to mid-December 2009, from mid-December 2009 to mid-November 2010, and from mid-November 2010 to October 2011. The error bars represent the standard error of the mean (SEM) for each year-long segment as will be explained in section 4b.

The variability in baroclinic structure is presented in relationship to bathymetry (Fig. 3). For example, the SFZ is at 58.5°S. Mean ϕ values decrease progressively southward, with the largest value of about 23 $m^2 s^{-2}$ at the northern slope of the section (C02 site). The SAF produces the gradient in mean ϕ north of 56.2°S (C05 site). The PF produces the gradient in mean ϕ between 57.2°S (C08 site) and roughly 60°S (C13 site). Meanders in these fronts produce the increased SEM and some interannual variability.

It is possible to identify two plateaus of nearly constant ϕ values, indicating the transition between the different fronts that compose the ACC: one with nearly constant mean ϕ values of about 20 $m^2 s^{-2}$ between 56.2° and 57.2°S and the other one approaching the southern boundary with nearly constant mean ϕ values of about 13 $m^2 s^{-2}$ between 60.4° and about 61.1°S.

The ϕ varies intra-annually (indicated by SEM bars) and interannually (indicated by the range of the four curves in Fig. 3). Comparing the four curves, we observe that the largest fluctuations (SEM) of the annual-mean ϕ exceed 0.4 $m^2 s^{-2}$ between about 55.5°S (C04 site) and 59.0°S (C11 site) and are associated with meanders of the SAF and PF and associated eddies. The fluctuations of the annual-mean ϕ are very small (less than 0.2 $m^2 s^{-2}$) south of 60°S. The largest interannual changes (of about 0.3–1.2 $m^2 s^{-2}$) are found between the SFZ at 58.5°S and approximately 60°S, also associated with interannual shifts of the PF.

b. *Time-variable ACC baroclinic transport*

Figure 4 shows the time series of the total baroclinic transport through Drake Passage and its components, the baroclinic transport at the northern slope, in the central passage section, and at the southern slope, calculated as outlined in section 3a. The basic statistics of the transport time series shown in Fig. 4 are displayed in Table 4. Unless otherwise noted, the reported variability represents one standard deviation.

The full across-passage total baroclinic transport (black line) mean and standard deviation between 3 December 2007 and 17 October 2011 is 127.7 ± 8.1 Sv. The minimum value is 92.2 Sv on 20 January 2010, while the maximum value is 150.1 Sv on 10 July 2008, yielding

TABLE 4. Basic statistics of baroclinic transport (Sv) through the northern slope (green line in Fig. 4), the central deep passage excluding the slopes (magenta line in Fig. 4), the southern slope (blue line in Fig. 4), the full Drake Passage (total baroclinic; black line in Fig. 4), carried by SAF and PF (SAF/PF; upper line in Fig. 8), and carried by SACCF (SACCF; lower line in Fig. 8). The mean and std dev of annual and average baroclinic transports are given in columns 3–7. The min and max values are given in columns 8–9. The SEM is given in column 10 (see section 4b for details of the calculation).

		Mean/std dev							
	Lat (S)	2008	2009	2010	2011	Avg	Min	Max	SEM
Northern slope	54°58.1′–55°36.0′	22.5/11.8	22.2/12.2	19.7/11.8	19.2/12.1	20.9/12.1	−10.1	66.5	1.6
Central deep passage	55°36.0′–61°43.4′	103.2/15.1	103.0/12.8	107.2/15.8	108.3/14.2	105.4/14.7	49.4	145.6	1.9
Southern slope	61°43.4′–61°57.7′	2.4/0.8	2.2/0.9	1.0/1.3	−0.1/1.7	1.4/1.7	−6.7	4.9	0.2
Total baroclinic	54°58.1′–61°57.7′	128.1/9.9	127.4/6.2	127.9/8.7	127.4/7.2	127.7/8.1	92.2	150.1	1.0
SAF/PF	54°58.1′–60°05.5′	108.6/9.3	106.3/8.0	103.2/8.0	100.6/8.3	104.7/8.9	65.1	131.1	1.1
SACCF	60°05.5′–61°57.7′	19.5/3.9	21.1/5.0	24.7/4.9	26.8/5.9	23.0/5.7	11.2	49.4	0.7

a transport range of about 58 Sv (almost half of its average). The annual-mean baroclinic transport and standard deviation (Table 4) for each deployment year of 128.1 ± 9.9, 127.4 ± 6.2, 127.9 ± 8.7, and 127.4 ± 7.2 Sv (years 2008, 2009, 2010, and 2011, respectively) is remarkably steady, as previously shown by Fig. 3.

The integral time scale is determined by the first zero crossing of the autocorrelation function of the total baroclinic transport time series. This yields an integral time scale of 12 days, indicating that every 24 days accumulates an independent estimate of the average. This results in about 60 effective degrees of freedom for the 4-yr record of baroclinic transport and an SEM of 1.0 Sv. To be conservative, we use 12 days as the integral time scale for all time series to compute the SEM (Table 4; column 10).

There is 20.9 ± 12.1 Sv of eastward flow along the northern slope above 3500 m (green line), indicating that about 15% of the total baroclinic transport occurs there. While on average the transport along the northern slope contributes 20.9 Sv, the transport range amounts to 77 Sv, including several times when the transport exceeds 50 Sv and a few times when it is negative (as low as −10 Sv). The arbitrary choice of end point at C03 leads to the occasional negative transport as meanders and eddies pass by the region. The large variability at the northern slope arises according to how much of the SAF shifts north of 55.36°S (C03 site), plus additional small-scale baroclinic waves and processes.

The flow in the central passage amounts to 105.4 Sv with a large variability of 14.7 Sv (magenta line) and a transport range of 96 Sv. Note the tendency for maxima and minima in the green and magenta curves to offset each other, resulting from the ACC fronts shifting between these two sections as they meander. The combined northern slope and central passage transport standard deviation is 8.6 Sv, thus reducing the variability of the full across-passage baroclinic transport by almost 40% compared to the variability without including the northern slope (of approximately 14.7 Sv standard deviation).

The transport along the southern slope (blue line) is much smaller than at the northern slope and amounts to only 1.4 Sv and fluctuates by ±1.7 Sv. The transport range is about 12 Sv, with the transport being mostly westward in the last year of the record. The latter is associated with eddies passing by the region.

Next, we examine the frequency distribution of the baroclinic transport. The total baroclinic transport time series displays markedly short-term variability. Transport fluctuations of about 35–55 Sv (from trough to peak) occur over periods as short as 2–3 weeks. For example, the transport increases by 41 Sv between 27 April and 11 May 2008, by 52 Sv between 20 January and 6 February 2010, and by 35 Sv between 20 October and 10 November 2010.

Spectra of the baroclinic transports are calculated using Welch's method with a 330-day Hamming window (Fig. 5). The spectrum of the total baroclinic transport has two significant peaks (at 95% confidence) near 20 days and near 55 days, with a red spectrum beyond 90 days (Fig. 5a). About 34% of the variance is associated with periods shorter than 30 days, and about 65% of the variance is associated with periods shorter than 60 days, indicating a large variability of the transport on monthly time scales and shorter.

The spectra of the baroclinic transport at the northern slope, in the central passage section, and at the southern slope are shown in Figs. 5b, 5e, and 5f, respectively. To further investigate the origin of the spectral peaks of each of these regions, the spectra of ϕ at the surface at the sites utilized as end points are also shown (Figs. 5c,d,g,h).

The frequency content of the total baroclinic transport (Fig. 5a) is mainly associated with the variability of ϕ at C02 (Fig. 5c). The total baroclinic transport and ϕ at C02 are well correlated ($r^2 = 0.84$, significant at 5% error probability), indicating that surface ϕ at C02 reflects a large fraction of the depth-integrated baroclinic

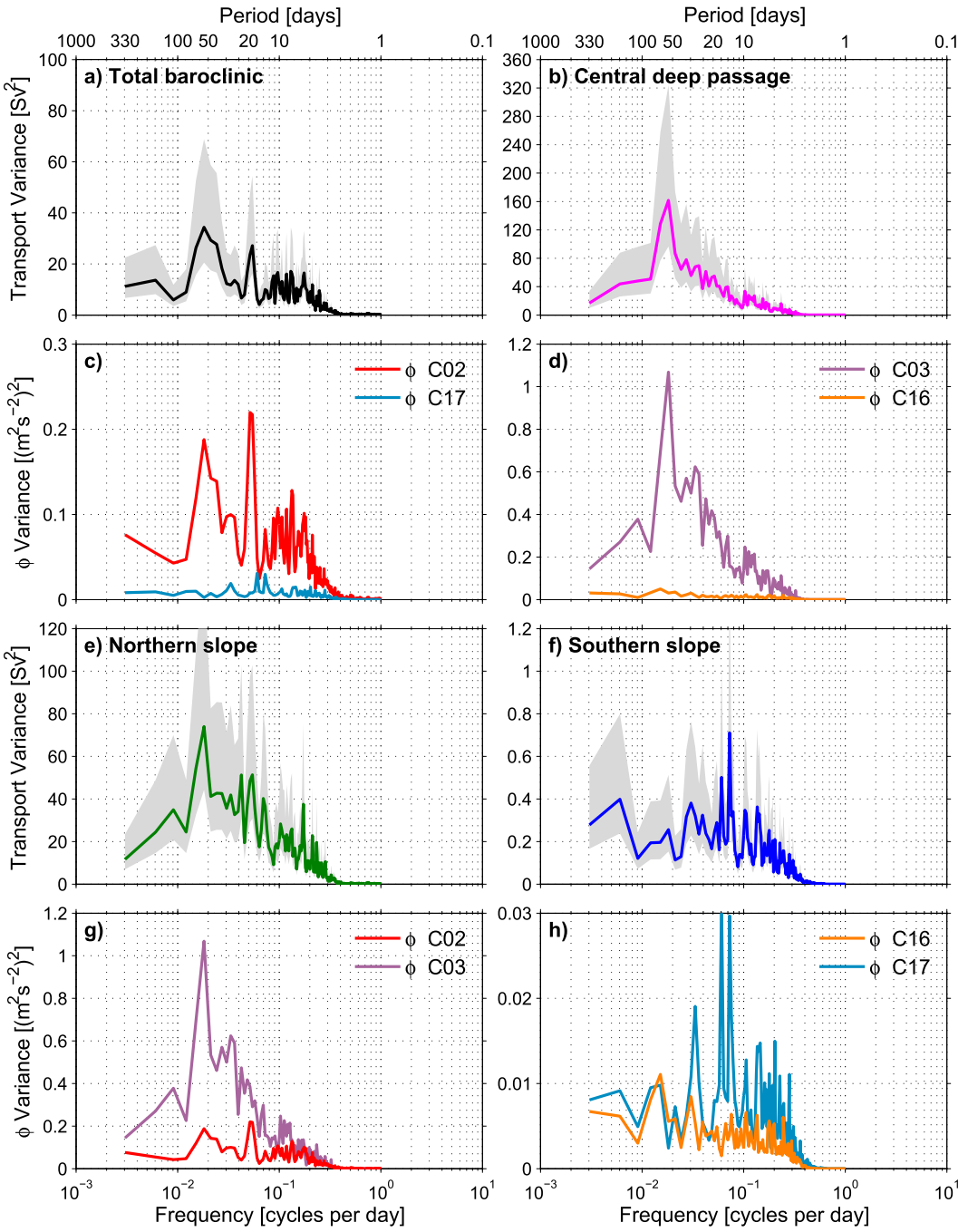

FIG. 5. Variance-preserving spectrum of (a) baroclinic transport time series and its constituents: (e) baroclinic transport at the northern slope, (b) in the central deep passage excluding the slopes, and (f) at the southern slope. Shaded confidence interval (95%) is also shown. The variance-preserving spectrum of ϕ at the surface relative to 3500 m (except at the southern slope where ϕ at the surface relative to 1260 m is evaluated) at the sites utilized as end points to compute each transport time series is shown at (c) C02 and C17, (d) C03 and C16, (g) C02 and C03, and (h) C16 and C17. For clarity, confidence intervals for the spectra of ϕ are not shown. The spectra are computed as detailed in section 4b. Note the different scales on the y axes.

flow changes. The highest correlation between the two time series ($r^2 = 0.88$) occurs for the 60-day high-pass-filtered records. Thus, for periods shorter than 60 days, the variability of surface ϕ at C02 explains 77% of the variance of baroclinic transport.

At the northern slope about 67% of the variance is associated with periods shorter than 60 days (Fig. 5e), indicating large short-term variability. The frequency content is associated with the variability from both ϕ at C02 and ϕ at C03 (Fig. 5g). Note that ϕ at C02 and ϕ at C03 are moderately correlated ($r^2 = 0.37$, significant at 5% error probability). The highest correlation between the two time series occurs for periods between 20 and 100 days ($r^2 = 0.45$). The ϕ at C02 and ϕ at C04 (about 80 km south of C02 and 40 km south of C03) are not significantly correlated, indicating that correlation scales are small approaching the northern slope.

The largest baroclinic transport variance occurs in the central deep passage associated mainly with meandering of the SAF across site C03 at the northern end. The spectrum has a distinct peak around 55 days and a not so well-defined peak around 20–30 days (Fig. 5b), which are largely associated with the ϕ variability at C03 (Fig. 5d). The variance in this region is largely balanced by that at the northern slope as the current shifts between the two regions. Thus, the variance of the total transport (Fig. 5a) is smaller than for these two contributing subregions, yet all have peaks near 20 and 55 days.

Noting that northern slope and central deep passage transport standard deviations (12.1 and 14.7 Sv, respectively) are larger than the total transport standard deviation (8.1 Sv), it seems natural to ask whether variability north of C02 might further reduce the total variability. We can estimate the standard deviation of transport sampled north of C02 by calculating the surface geostrophic velocity between M01 and C02 and convert that velocity standard deviation to a transport standard deviation by using the mean shear structure between C01 and C02 (section 3a). Recall that M01 is located 6 km south of C01. Our approach in estimating the full 4-yr baroclinic transport variability has been to use the best northernmost τ record available. The standard deviation of this baroclinic transport north of C02 is 1.3 Sv. Three processes likely contribute to this small standard deviation: coastally trapped waves (CTW), SAF meanders north of C02, and noise from the M01 pseudo-IES τ_{cm} estimates. CTW would presumably average to zero, while SAF meanders would rectify, each northward meander crest adding to the mean transport north of C02. While we do not know the partitioning of these processes, we can say that the sum is small, 1.3 Sv compared to 8.1 Sv of the total transport standard deviation, and only a fraction of the 1.3 Sv might oppose the 8.1-Sv variability south of C02.

At the southern end, the spectrum (Fig. 5f) is nearly two orders of magnitude smaller than observed at the northern slope. This indicates that the baroclinic shear is very weak at the southern end of Drake Passage. Unlike the other regions, higher-frequency fluctuations dominate the spectrum. Two distinct peaks occur near 14 and 33 days, and these are predominantly associated with the ϕ variability at C17 (Fig. 5h). The 50–80-day broad peak that is so prominent in the other regions is much reduced here.

The total across-passage baroclinic transport is determined by the northern and southern end points. A comparison of the spectra in Figs. 5c and 5d clearly shows that the most energetic fluctuations occur across the whole spectrum at the northern end of the passage.

c. *Implications for satellite altimeter sampling at 10-day interval*

Satellite altimetry provides a useful tool to estimate the time-variable strength of upper-ocean velocities, as a basis for future monitoring of the ACC. Here we address one potential complicating factor: aliasing of high-frequency variability due to the insufficient temporal resolution of the 10-day repeat cycle of the Jason and Ocean Topography Experiment (TOPEX)/Poseidon altimeters, which has a Nyquist frequency of 1 cycle per 20 days. Temporal aliasing results when a continuous signal is subsampled at discrete times. Periodicities shorter than 20 days are aliased and appear as if they contributed to lower-frequency variability, thus complicating the interpretation of the satellite data. Altimeter products exist that map SSH to finer temporal resolution than observed, for example, Archiving, Validation, and Interpretation of Satellite Oceanographic data (AVISO) products are typically mapped at 7-day intervals and even daily maps have been produced. Yet it is important to note that mapping to higher temporal resolution (even when data from multiple satellites are included) does not change the intrinsic sampling resolution of the measurement system. Considerable effort is taken to account for high-frequency dynamic oceanic variability that is poorly sampled by the altimeter measurements. For example, AVISO uses a barotropic model to determine the response of a barotropic ocean to high-frequency wind and atmospheric forcing. Gille and Hughes (2001) examined aliasing of the barotropic component from bottom pressure records in Drake Passage. They found for periods between 20 and 40 days that aliased bottom pressure variance exceeds that of the resolved signals. We are unaware of any corrections for high-frequency baroclinic signals, despite a variety of high-frequency baroclinic processes along the northern slope, such as internal tides, topographic and shelf wave

processes, and short-period eddies that contribute variability at periods shorter than 20 days (at the northern slope, 27% of the variance in baroclinic transport is associated with periods shorter than 20 days; Fig. 5e).

Using the hourly records of τ and the corresponding baroclinic transport time series, recognizing that low-pass filtering would be required to interpret the geostrophic variability, we can simulate 10-day sampling and test how much energy is aliased into low frequencies. Following the methodology of Gille and Hughes (2001), we subsample the hourly record of the baroclinic transport at 10-day intervals and compute the spectrum. We iterate the calculation for the subsampled time series, offsetting the time series by one time step, until the spectra have been computed for every data point in the 10-day interval. Here, we use only the transport record calculated with the C02 τ record (excluding the pseudo-IES values). Spectra are computed using the Welch method with a 330-day Hamming window. We split the record into a year-long segment plus a 2-yr-long segment and apply this procedure for each segment of the record, followed by ensemble averaging all the subsampled spectra (solid black line in Fig. 6a). Spectra from the subsampled data (open squares) have more energy for frequencies lower than the Nyquist frequency of 1 cycle per 20 days compared to the spectrum of hourly data (solid black line). In particular for baroclinic transport calculations, the fraction of spectral energy associated with periods shorter than 20 days is about 28%. This implies that about 28% of apparent energy in the subsampled spectral estimates at periods longer that 20 days results from aliasing.

The fraction of aliased energy as a function of frequency is shown in Fig. 6b [defined as 1 minus the ratio of the energy in the spectrum computed from the hourly record of baroclinic transport to the energy in the spectra computed from the subsampled record following Gille and Hughes (2001)]. For periods longer than 40 days, less than 40% of the energy has been aliased. For periods between 40 and 20 days, the fraction of aliased energy increases substantially to between 40% and 80%. In consequence, the spectra computed from 10-day repeat measurements of the baroclinic contribution to SSH will only be representative of long-period variability (periods long compared to 40 days).

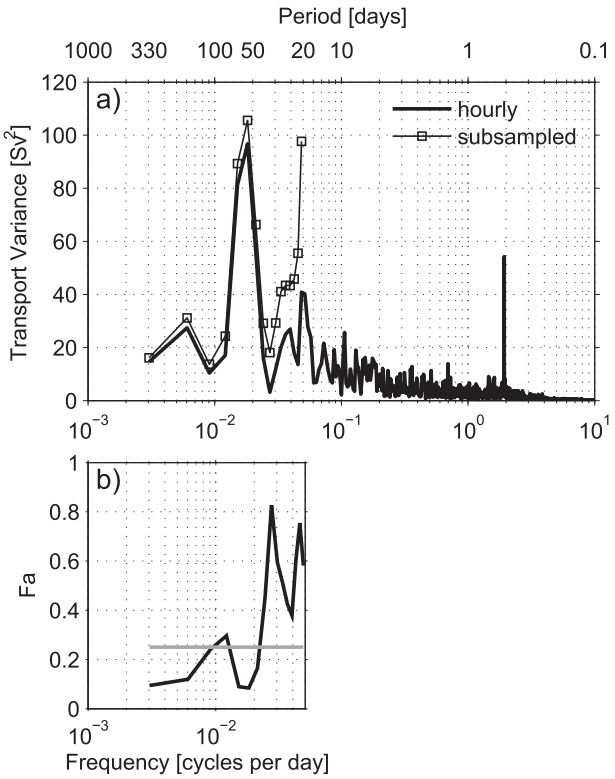

FIG. 6. (a) Variance-preserving spectrum of hourly record of baroclinic transport (black line) and of hourly record of baroclinic transport subsampled at the 10-day repeat cycle of the Jason altimeter computed as detailed in section 4c (open squares). (b) Fraction of aliased energy Fa in spectrum computed from baroclinic transport subsampled into 10-day intervals. The gray horizontal line represents the limit of one-quarter of the energy being aliased.

d. ACC baroclinic transport distributed among fronts

The distribution of the baroclinic transport between each CPIES pair versus time and latitude in Fig. 7 shows the time-varying position of the ACC fronts. We observe on any given day that the high transport tends to be concentrated in three regions: near 56°S, 58.5°S, and south of 60°S. In addition, surface ϕ contours that coincide with the maximum mean ϕ gradient (Fig. 3) in the frontal regions found at the SAF, PF, and SACCF (bold lines) are overlain on baroclinic transport. Regions of strong transport often merge together, are not consistently associated with a single ϕ contour, and are strongly influenced by topography.

While the mean SAF is found along the northern slope, it frequently meanders southward. Large SAF meanders can extend to 58°S, for example, February and April–May 2008 (Fig. 7a), from mid-April to mid-May 2009 (Fig. 7b), and April–May 2010 (Fig. 7c). During these periods, the SAF and PF are merged into a single front. Regions of strong negative transport along the mean SAF contour that occur north of 58°S indicate intervals when the SAF folds back on itself in an "S"-shaped meander, for example, July 2009, April 2010, and February 2011 (Figs. 7b,c,d).

The strongest eastward transports tend to occur when the PF is near the SFZ at 58.5°S (C10), but there are times when the PF migrates farther south near 60°S

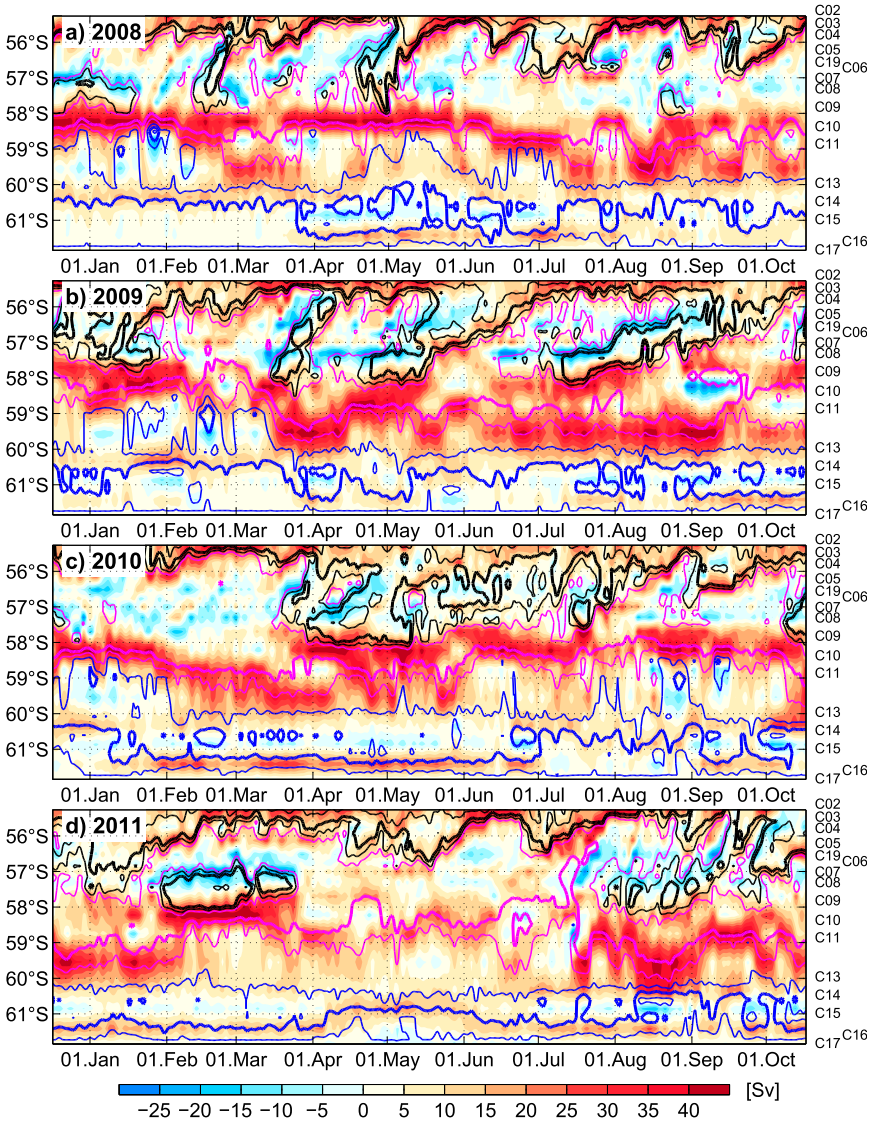

FIG. 7. Hovmöller diagram of 72-h low-pass-filtered baroclinic transport (Sv) in Drake Passage as a function of time and lat for each deployment year: (a) 2008, (b) 2009, (c) 2010, and (d) 2011. To facilitate interannual comparison, the same dates for the beginning and end for each deployment year are chosen. The thick overlaid contours indicate the values of the surface ϕ streamlines ($m^2 s^{-2}$) associated with the max mean ϕ gradient for each frontal region from Fig. 3: SAF (black), PF (magenta), and SACCF (blue). The thin overlaid contours represent the max and min values of ϕ for each frontal region from Fig. 3. Labels on the right indicate names of the CPIES sites.

(C13). For instance, in the first half of 2008, the position of the PF is persistently located mostly between 58° and 59°S (C09 and C10; Fig. 7a), while between June and October 2009 (Fig. 7b), October–November 2010 (Fig. 7c), and August 2011 (Fig. 7d), the PF is located farther south between roughly 59° and 60°S (C11 and C13). From our measurements, the PF is not readily identified by a single ϕ contour; instead, the ϕ contour that identifies the PF appears to depend on whether the PF is north or south of the SFZ (C10).

Near the southern end of Drake Passage, a local maximum baroclinic transport occurs, mostly south of 60°S associated with the SACCF. The SACCF has a bimodal distribution occurring either near 60.3°S between C13 and C14 or, more frequently, near 61.4°S between C15 and C16. Similar to the PF, the ϕ that identifies the strongest gradient depends upon latitude. For example, in mid-January and early February 2009, when the transport maxima are near 60.3°S, it is collocated with the mean SACCF ϕ, while from mid-July through

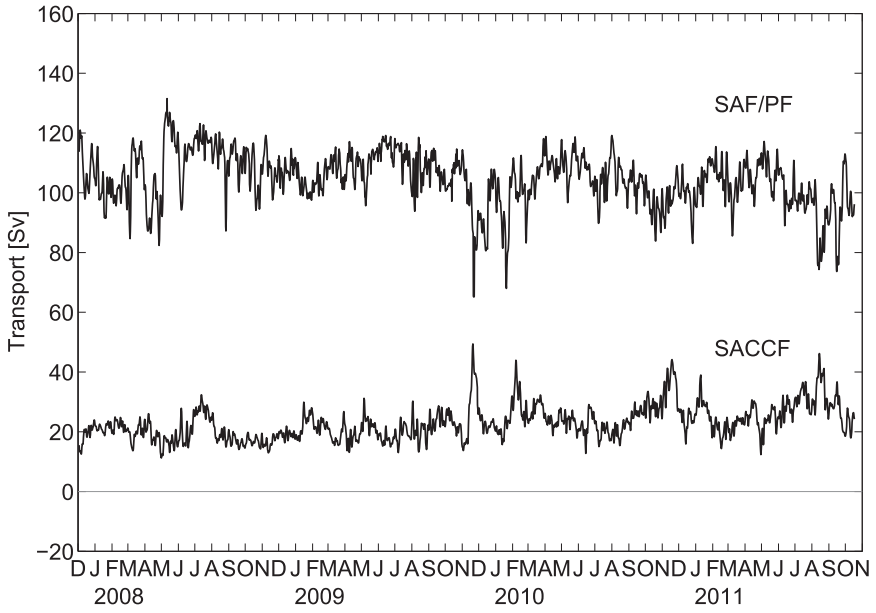

FIG. 8. Partition of 72-h low-pass-filtered baroclinic transport carried by the combined SAF and PF and that carried by the SACCF.

November 2009, when the transport maxima are near 61.4°S, it is collocated with a lower ϕ.

We report the time-varying baroclinic transport carried by the combined SAF and PF because they are not readily separable: SAF meanders reach as far south as 58°S, and at times the SAF and PF merge together. Note that using a specific ϕ contour to demark the boundaries of a front would simply lead to a constant transport. We compute the transport between the northernmost end of the section (C01) and nearly 60°S (C13). The SAF and PF together carry 104.7 ± 8.9 Sv (standard deviation) with a range of 66 Sv (SAF/PF; upper line in Fig. 8; Table 4), accounting for about 80% of the mean total baroclinic transport through Drake Passage. South of 60°S, the SACCF carries 23.0 ± 5.7 Sv with a range of 38 Sv (lower line in Fig. 8; Table 4). The SAF/PF and SACCF time series exhibit partially compensating changes. Figure 7d shows that the PF and SACCF are in close proximity in both the early and later parts of 2011 and farther apart in midyear. Times when the SACCF transport exceeds 40 Sv indicate sporadic migrations of the PF farther south up to the end point used for the calculation near 60°S (C13) (e.g., August 2011; Fig. 7d).

e. ACC baroclinic transport in neutral density layers

Here, we investigate the baroclinic transport of individual water masses through Drake Passage. Figure 9 shows a section of γ^n computed following Jackett and McDougall (1997) from the CPIES distributed across Drake Passage on a selected date. The γ^n section is characterized by density surfaces that slope upward toward the south. As defined in section 3a, we consider four water masses: SASW/AAIW ($\gamma^n < 27.5\,\mathrm{kg\,m^{-3}}$), UCDW ($27.5 < \gamma^n < 28.0\,\mathrm{kg\,m^{-3}}$), LCDW ($28.0 < \gamma^n < 28.2\,\mathrm{kg\,m^{-3}}$), and AABW ($\gamma^n > 28.2\,\mathrm{kg\,m^{-3}}$).

The time series of the geostrophic transports for baroclinic velocities relative to the bottom classified according to γ^n layers are shown in Fig. 10 (bottom). Their basic statistics are displayed in Table 5. The largest transports are found in the density classes of UCDW (57.5 ± 3.1 Sv), followed by SASW and AAIW (39.2 ± 4.0 Sv), LCDW (27.7 ± 2.1 Sv), and AABW (3.3 ± 1.1 Sv). The variability in AABW is quite large compared to its mean value, and the time series in Fig. 10 shows that pulses of higher transport occur episodically. The layer transport variability decreases with depth, with the largest variability found in waters lighter than $\gamma^n = 27.5\,\mathrm{kg\,m^{-3}}$. The upper three water masses are vertically coherent. Visual inspection reveals that the periods of relatively high or low total baroclinic transport [Fig. 10 (top)] are mostly associated with changes affecting the density classes of SASW/AAIW, UCDW, and LCDW, increasing upward with the baroclinic velocity profile. This is not surprising given that the density class of AABW is mainly present south of the SFZ with occasional intrusions north of the SFZ.

The steady, annual-mean, baroclinic transport in layers implies no interannual change in the flow associated with any particular water mass (Table 5).

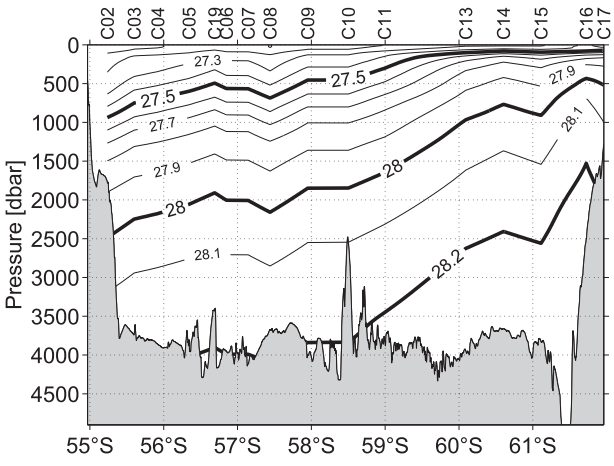

FIG. 9. Section of neutral density (γ^n; kg m^{-3}) from CPIES distributed across Drake Passage on 16 Mar 2010. Thick contours represent water mass limits: SASW and AAIW lighter than 27.5; UCDW 27.5–28.0; LCDW 28.0–28.2; and AABW denser than 28.2. Contour intervals are 0.1 kg m^{-3}. Labels at the top indicate names of the CPIES sites.

5. Comparison with previous ACC baroclinic transport estimates

How do our estimates compare with previous transport estimates from hydrography? Published estimates of baroclinic transport through Drake Passage have used different depths and methods. The reported ISOS transports (Whitworth 1983; Whitworth and Peterson 1985) cannot be unambiguously separated into our baroclinic framework; therefore, no comparisons with the ISOS values are made. Instead, we compare our analyses to those that used comparable methods (Table 6).

Cunningham et al. (2003) combined seven hydrographic sections at the western end of the passage between 1975 and 1980 with six WOCE SR1b sections between 1993 and 2000. The combined sections gave 107.3 ± 10.4 Sv baroclinic transport relative to and above 3000 m between 1975 and 2000. Using only the six SR1b sections, their transport relative to 3000 m was 112.7 ± 5.2 Sv with a range of 105–118 Sv. Our mean transport estimate recalculated using the same reference level is 100.4 ± 6.0 Sv with a range of 75–117 Sv, about 12 Sv smaller than their mean estimate between 1993 and 2000. The full-depth mean baroclinic transport estimate from just the six SR1b sections was even higher at 136.7 ± 7.8 Sv with a range of 123.1–143.8 Sv between 1993 and 2000 (Cunningham et al. 2003).

However, additional SR1b sections taken between 2007 and 2011 yield full-depth mean transport of 127.9 ± 8.0 Sv, which agree well in Fig. 10 with the cDrake time series mean of 127.7 ± 8.1 Sv (Tables 4 and 6). It is plausible that the short-period variability observed in cDrake might not be correlated with variations at SR1b, with the difference arising from coastal baroclinic features of alongstream scale shorter than the separation between cDrake and SR1b. Moreover sampling methodology and the 5–8-day time interval required to complete the SR1b CTD transect could account for differences of at least 2 Sv. Hence, we conclude that the mean values from cDrake and SR1b, which differ by only 0.2 Sv, agree well within the SEM for the five SR1b transects ($8.1/\sqrt{5-1} = 4$ Sv).

The comparison of the baroclinic transport in γ^n layers from cDrake and SR1b between 2007 and 2011 is shown in Table 5. Both the means and the variability of the layer transports from the two transects are consistent with each other within each of the four layers considered here.

Other hydrographic sections have estimated baroclinic transports in Drake Passage in 2003–06. Koshlyakov et al. (2007) occupied sections in 2003 and 2005 along a line crossing the SFZ close to the cDrake array. Their baroclinic transport relative to the bottom was 122 and 130 Sv. In 2006, Renault et al. (2011) occupied two sections east of cDrake and west of SR1b. They evaluated baroclinic transport relative to the bottom, finding 150.5 and 136.3 Sv. All these individual measurements fall within the range observed in our time series.

6. Discussion and summary

The 4-yr-long full-depth ACC baroclinic transport time series has a mean strength of 127.7 ± 1.0 Sv (standard error) and a temporal standard deviation of 8.1 Sv, with a large transport range of about 58 Sv. Transport variations of about 40 Sv or more occur in periods as short as 2–3 weeks. The annual-mean transport is remarkably steady during the 4 yr of measurements.

The cDrake array was highly resolved both spatially and temporally. A careful error analysis has shown that the errors for all the transport time series presented here are small (section 3b; Table 3). In particular for the full-passage ACC baroclinic transport, we obtain error estimates of 11.9 and 5.9 Sv for 72-h and >10-day low-pass-filtered records, respectively. Our results show that the combination of the CPIES τ measurements with the GEM tables provides an excellent method for estimating the ACC baroclinic transport and its variability through Drake Passage.

We have shown that a large part of the variance (65%) in our estimate of ACC baroclinic transport is associated with periods shorter than 60 days, demonstrating the short-term variability in the record. The spectrum has two peaks near 20 and 55 days. The dynamical drivers of these spectral peaks are currently being investigated.

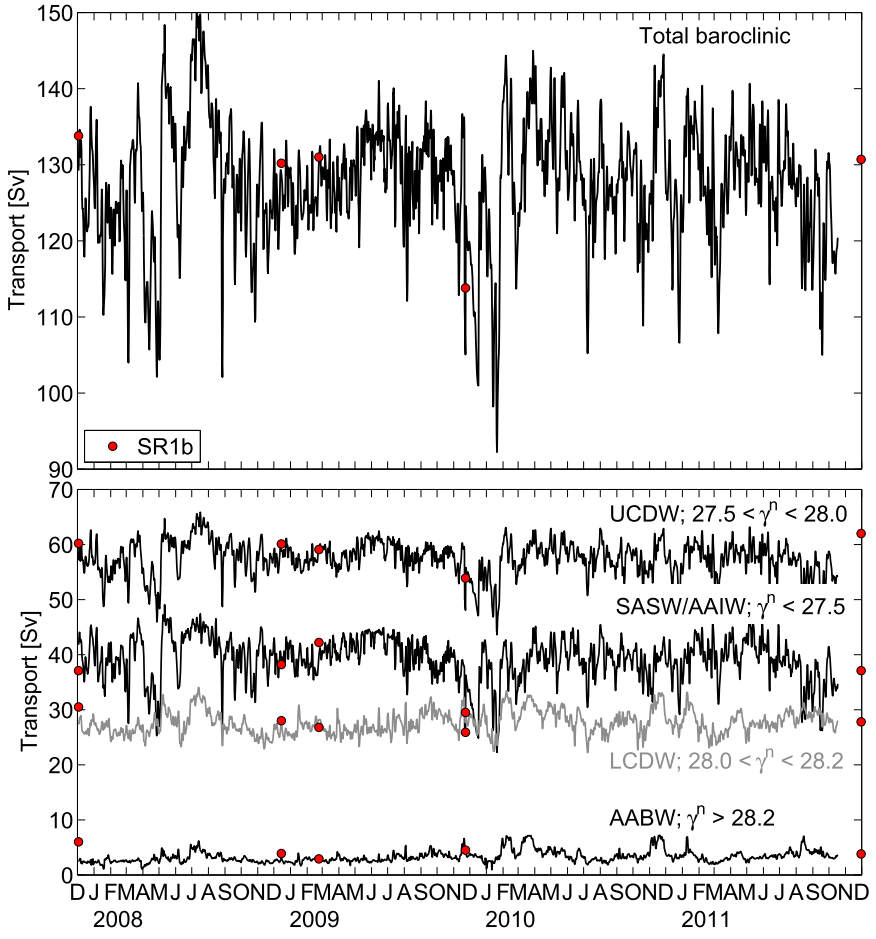

FIG. 10. (bottom) Time series of 72-h low-pass-filtered baroclinic transport through Drake Passage integrated in neutral density layers (γ^n; kg m^{-3}): SASW and AAIW lighter than 27.5; UCDW 27.5–28.0; LCDW 28.0–28.2; and AABW denser than 28.2. (top) The sum of the four layers (total baroclinic) is added for comparison (identical to the total transport shown in Fig. 4, note the change of the transport scale on the *y* axis). Overlaid on top are the five samples at the WOCE SR1b line (red dots).

Our analysis indicates that the baroclinic transport variability is dominated by density stratification variations at the northern slope of the section. Near-boundary processes close to the northern slope such as coastal, topographic and Kelvin-propagating waves, small-scale eddy variability, or locally forced motions such as wind-driven Ekman pumping may play a significant role in determining the observed fluctuations of the baroclinic transport.

Our results show that energetic high-frequency variability in the hourly spectrum of baroclinic transport, when subsampled at the 10-day repeat cycle of the Jason altimeter, is aliased to lower frequencies, particularly for periods between 20 and 40 days. These results complement the findings of Gille and Hughes (2001), who examined the barotropic (deep bottom pressure) component. It is likely that a correction to the steric signal in the altimeter measurements would be necessary to eliminate aliased high-frequency energy in the attempt to use altimetry for future ACC monitoring efforts.

The transport carried by the SAF and PF together amounts to 80% of the total baroclinic transport. From our observations, in general, three distinct regions associated with maxima in baroclinic transport are observed at any given time in Drake Passage. Sokolov and Rintoul (2009a) identified multiple frontal branches and concluded that if a front occurs it tends to occur at a specific SSH contour (or geopotential height ϕ contour). This is consistent with our analysis. We find that the ϕ most closely associated with the three fronts can change from day to day, but specific ϕ values tend to be favored (PF and SACCF, in particular). The SAF is a bit more complex because an "S"-shaped meander is often

TABLE 5. Mean and std dev of baroclinic transport (Sv) relative to the bottom in neutral density layers. Column 1 indicates the water masses and column 2 indicates their neutral density range (γ^n; kg m^{-3}): SASW and AAIW lighter than 27.5; UCDW 27.5–28.0; LCDW 28.0–28.2; and AABW denser than 28.2. Columns 3–7 indicate the mean and std dev of annual and average layer transports from cDrake. The average transports in γ^n layers relative to the bottom from five hydrographic sections (between 2007 and 2011) at the WOCE SR1b line are displayed in column 8. The sum of layer transports is shown in the final row (agreeing with Table 4). Regarding the listed std dev error bars, because the number of degrees of freedom of the cDrake estimates is about 15 yr^{-1}, the SEM estimates would be reduced by a factor of 4 compared to the values listed.

		cDrake mean/std dev					
Water mass	γ^n (kg m^{-3})	2008	2009	2010	2011	Avg	SR1b mean/std dev
SASW/AAIW	<27.5	40.0/4.6	39.5/3.6	38.5/3.7	38.7/3.9	39.2/4.0	36.8/4.6
UCDW	27.5–28.0	57.9/3.9	57.7/3.7	57.3/2.4	57.1/2.9	57.5/3.1	59.1/3.1
LCDW	28.0–28.2	27.3/2.1	27.2/1.7	28.3/2.3	28.0/1.9	27.7/2.1	27.8/1.7
AABW	>28.2	2.9/0.8	3.0/0.7	3.8/1.4	3.6/1.0	3.3/1.1	4.2/1.1
		128.1/9.9	127.4/6.2	127.9/8.7	127.4/7.2	127.7/8.1	127.9/8.0

present in northern Drake Passage, and the SAF and PF merge and separate within this region. Thus, our measurements show that at this particular location in Drake Passage, it is not possible to uniquely separate the SAF from the PF at all time steps; there is neither a single latitude separating the two fronts nor are there ϕ streamlines systematically associated with the local maxima in baroclinic transport.

We evaluated transports in four neutral density layers. The largest transports are found in the density class of UCDW, while the smallest transports are found in the density class of AABW. Layer transports are statistically steady.

The baroclinic transport estimates obtained from the occasional hydrographic sections at the downstream SR1b line can be compared with the 4-yr continuous cDrake estimates. From sections prior to 2000, Cunningham et al. (2003) estimated mean baroclinic transports about 9 Sv higher than cDrake. Preliminary evidence from that suite of sections (not shown here) is that mean SR1b transports within the four layers (SASW/AAIW, UCDW, LCDW, and AABW) are consistently higher than cDrake. This offers a promising topic for future investigation. The 9-Sv change in the total exceeds twice the standard error of the mean estimates. It indicates that the observed decrease in baroclinic transport between the decades 1993–2000 and 2007–11 is statistically significant at the 96% confidence level. For our present purposes, recall from Table 6, however, the contemporaneous SR1b estimates between 2007 and 2011 agree well with the

TABLE 6. Baroclinic transport through Drake Passage (Sv) relative to and above the reference level indicated in column 3. Column 1 indicates the reference from which the information in columns 2–5 was taken. Values in column 4 indicate the mean and std dev. The cDrake estimates are given in the final two rows.

Author	Dates	Reference level (m)	Baroclinic transport mean/std dev	Notes
Cunningham et al. (2003)	1975–2000	3000	107.3/10.4	Hydrography western end passage (7 sections) and SR1b (6 sections)
	1993–2000	3000	112.7/5.2	SR1b (6 sections)
		bottom	136.7/7.8	SR1b (6 sections)
Koshlyakov et al. (2007)	2003	bottom	122	1 section
	2005	bottom	130	1 section
Renault et al. (2011)	2006	3000	117.0	DRAKE (1 section)
		bottom	150.5	DRAKE (1 section)
	2006	3000	103.0	DRAKE (1 section)
		bottom	136.3	DRAKE (1 section)
This study	2007–11	bottom	127.9/8.0	SR1b (5 sections)
	November 2007–October 2011	3000	100.4/6.0	cDrake CPIES (72-h low-pass filtered)
		bottom	127.7/8.1	cDrake CPIES (72-h low-pass filtered)

cDrake estimates, both in the mean and the variability. These results are suggestive of long-term variability in the baroclinic transport through Drake Passage that points to the need for sustained monitoring.

Our results reinforce the idea that full-depth ACC baroclinic transport variability is significant. Cunningham et al. (2003) reexamined the ISOS results and estimated that the ratio between total transport variability and baroclinic transport variability relative to and above 2500 m was 9.9/5.5 Sv. During the 4-yr cDrake experiment, we find that baroclinic transport variability using the same reference level is 4.8 Sv (not shown), which compares well with that reported for the ISOS results. Full-depth ACC transport variability from cDrake (8.1 Sv) is nearly twice as large as that above 2500 m. Efforts are underway to use the deep pressure and current-meter measurements from cDrake to provide the reference velocity to obtain the total ACC transport.

Ongoing work seeks to identify and understand the dominant physical driving mechanisms of the baroclinic transport fluctuations described here.

Satellite altimeter measurements are likely to be part of future ACC monitoring efforts in Drake Passage. Cunningham and Pavic (2007) successfully combined surface velocity anomalies from satellite SSH with measured surface currents from seven SR1b sections to obtain the total surface geostrophic velocities across the ACC between 1992 and 2004. From our measurements, a simple estimate of the meridional surface geopotential ϕ gradient just using ϕ time series at the northern (C02) and the southern (C17) end points of the passage explains about 65% of the total baroclinic transport variance (not shown), indicating that the boundary-to-boundary gradient in surface ϕ is representative of a large fraction of the depth-integrated baroclinic transport changes. In situ measurements of ϕ at the surface can be taken as a proxy for the steric signal in the altimeter measurements. If good agreement was found between our CPIES-derived surface ϕ and satellite SSH at the northern and southern end points in Drake Passage, SSH could be used to infer a large fraction of the variability of the baroclinic transport for periods longer than 20 days. Care should be taken with the interpretation of potentially aliased high-frequency signals to lower frequencies in the altimeter measurements (section 4d). Different satellite products will be evaluated and techniques for using satellite SSH to infer ACC baroclinic transport will be tested.

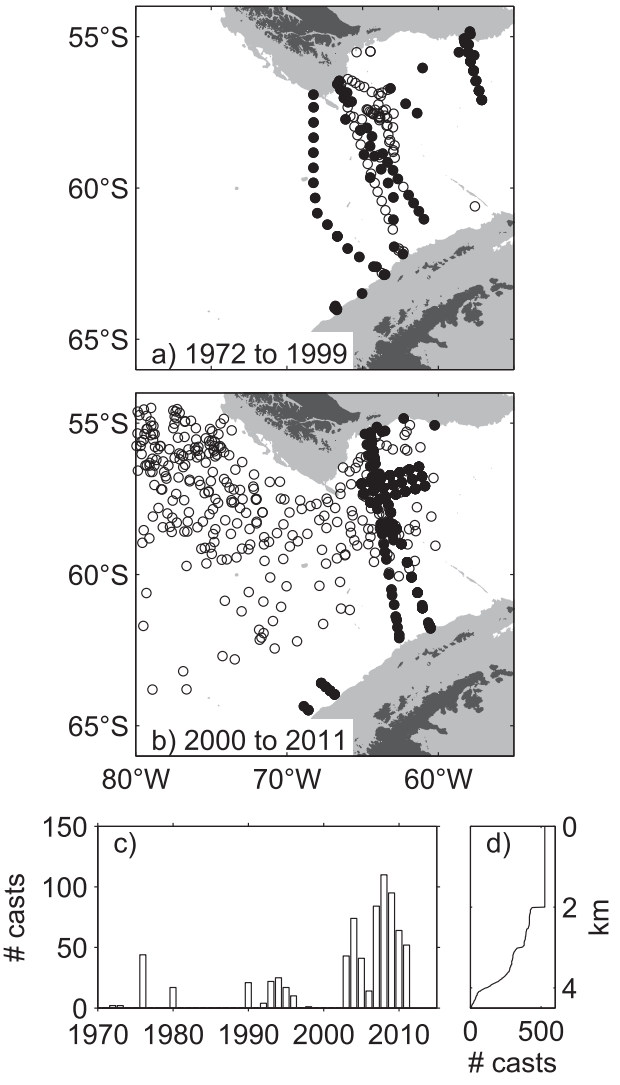

FIG. A1. Spatial and temporal distribution of the CTD and Argo profiles used to construct the cDrake GEM lookup tables. (a) Circles indicate the location of profiles taken between 1972 and 1999. Solid circles indicate casts that reached within 200 dbar of the seafloor. Water depths shallower than 2000 m are shaded gray. (b) As in (a), but for profiles taken between 2000 and 2011. (c) Distribution of casts by year. (d) Distribution of T and S measurements by depth.

Acknowledgments. The National Science Foundation Office of Polar Programs supported this work under NSF Grants ANT-0636493 (SIO cDrake) and ANT-0635437/ANT-1141802 (URI cDrake). We are very grateful to Teri Chereskin for coleading the cDrake project and for many helpful discussions. We thank the two anonymous reviewers for their thoughtful comments and suggestions, which improved this manuscript. We gratefully acknowledge the captains and crew of the RVIB *Nathaniel B. Palmer* and the staff of Raytheon Polar Services for their support during the seagoing activities. We thank Erran Sousa, Gerard Chaplin, and Dan Holloway for their valuable help in the CPIES instrumentation development and preparation.

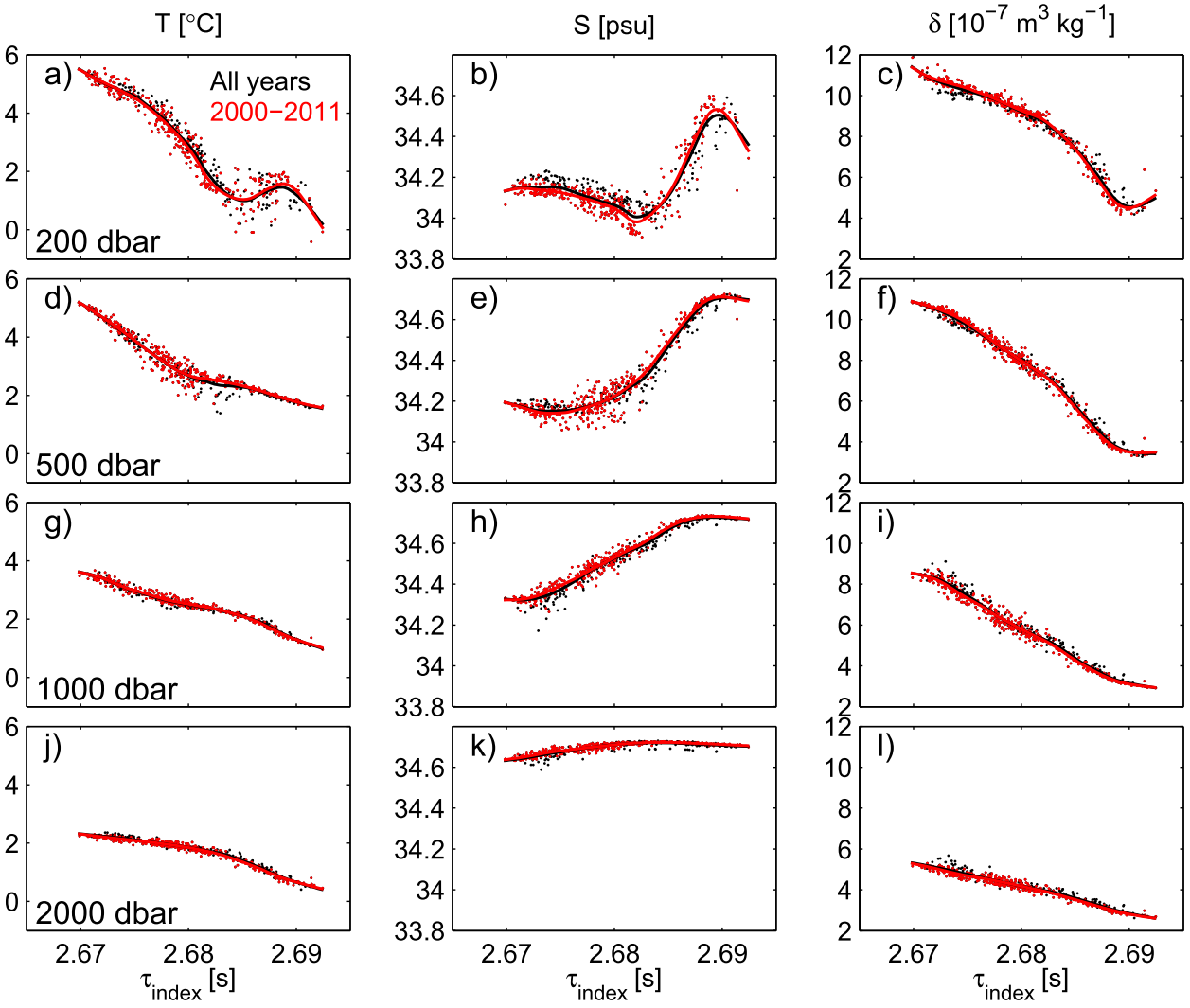

FIG. A2. Comparison of hydrographic casts (dots) and the fitted spline curves for two cases: all data from 1972–2011 (black) and just the data from 2000–11 (red). Temperature, salinity, and specific volume anomaly are shown for four levels.

The U.K. Natural Environment Research Council funded the SR1b section occupations used in this work through several core strategic research programs at the National Oceanography Centre Southampton and the British Antarctic Survey.

APPENDIX

cDrake GEM

The cDrake GEM lookup tables were discussed in section 2c. Here additional details about spatial and temporal distribution of the hydrographic casts used to construct the GEMs are presented and the robustness of the GEMs is demonstrated.

The spatial and temporal distributions of the CTD and Argo float profiles reaching to 2000 dbar or greater are shown in Fig. A1. The histogram in Fig. A1c illustrates that the majority of the casts were taken after 2000, primarily due to the availability of Argo floats. The locations of casts pre- and post-2000 are displayed separately. Of the 526 total casts, 326 reached within 200 dbar of the seafloor at their location (solid black circles). Of the 281 casts reaching to 3500 dbar or greater, 203 were taken on the cDrake cruises between 2007 and 2011.

Recent studies have shown that some changes have occurred over time in ACC water properties. However, because there are only a relatively small number of deep-reaching casts in this region, we have chosen to include all casts regardless of the year in which they were taken. To illustrate that the inclusion of data from

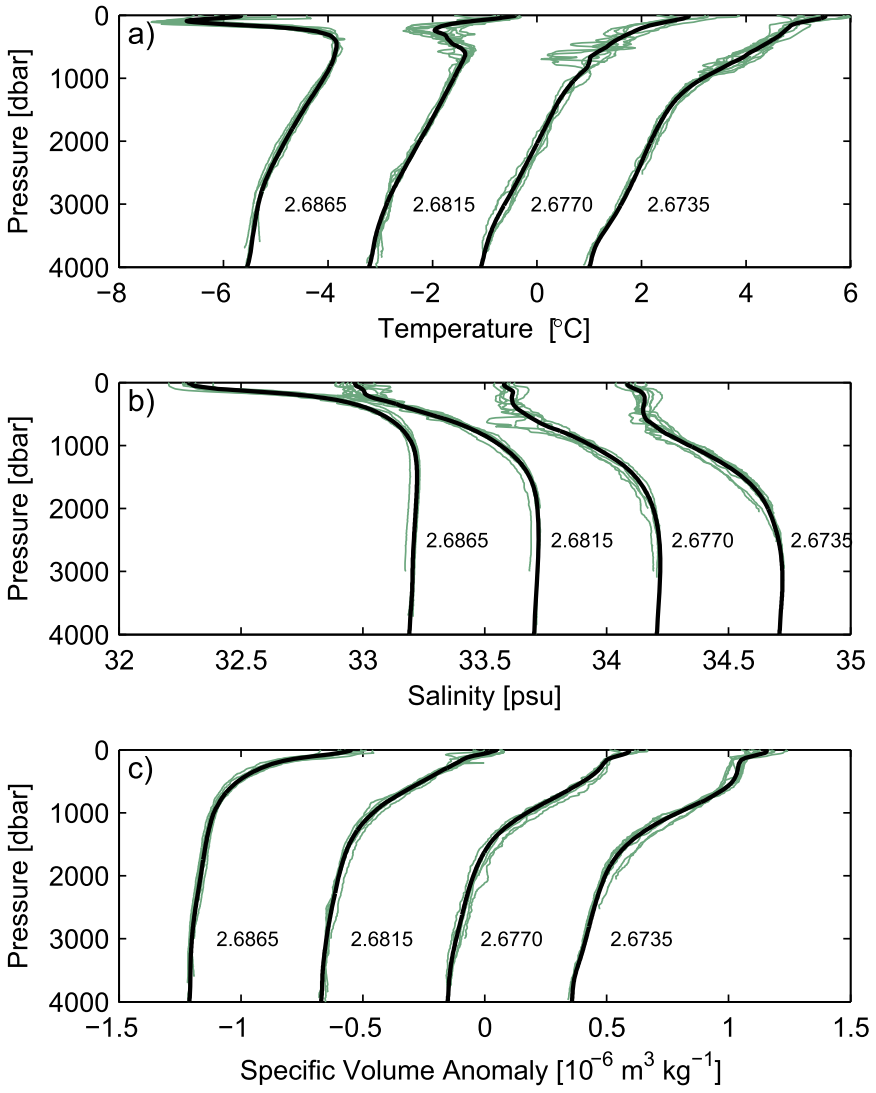

FIG. A3. (a) Four clusters of temperature profiles, each showing all the hydrocast profiles (light green lines) for which the travel time τ values are within $\pm 0.000\,25$ s of the values labeled (nominally 0.004 s apart). The GEM temperature profile at the corresponding τ is shown by the black line. The rightmost set of profiles has no temperature offset, and the remaining clusters have been offset to the left by increments of 2°C. (b) As in (a), but for salinity profiles; clusters are offset left by 0.5 psu. (c) As in (a), but for specific volume anomaly δ profiles; clusters are offset left by $0.5 \times 10^{-6}\,\mathrm{m^3\,kg^{-1}}$.

multiple decades has little to no effect on our transport calculations, we calculated a second set of GEM lookup tables using only the subset of casts taken between 2000 and 2011. Figure A2 superimposes the fitted spline curves of the cDrake GEMs (black lines) and those created with the data subset (red lines). Small differences between the fits are evident for T and S at the upper three depths. However, these differences have an insignificant effect on δ; for example, the δ curves at 200 dbar differ by less than $0.2 \times 10^{-7}\,\mathrm{m^3\,kg^{-1}}$. Consequently, geopotential ϕ and baroclinic transport calculated from δ are also unaffected by these small, interdecadal T and S differences.

Next, we show that the GEM fields capture the dominant vertical structure through the water column. Four clusters of T, S, and δ profiles are shown in Fig. A3. The four τ groupings, separated nominally by 0.004 s, span nearly the full τ range of the GEMs. These specific values were selected because multiple deep-reaching casts fell within each τ cluster. The vertical structure varies substantially between the four clusters, and these differences are captured by the GEM profiles.

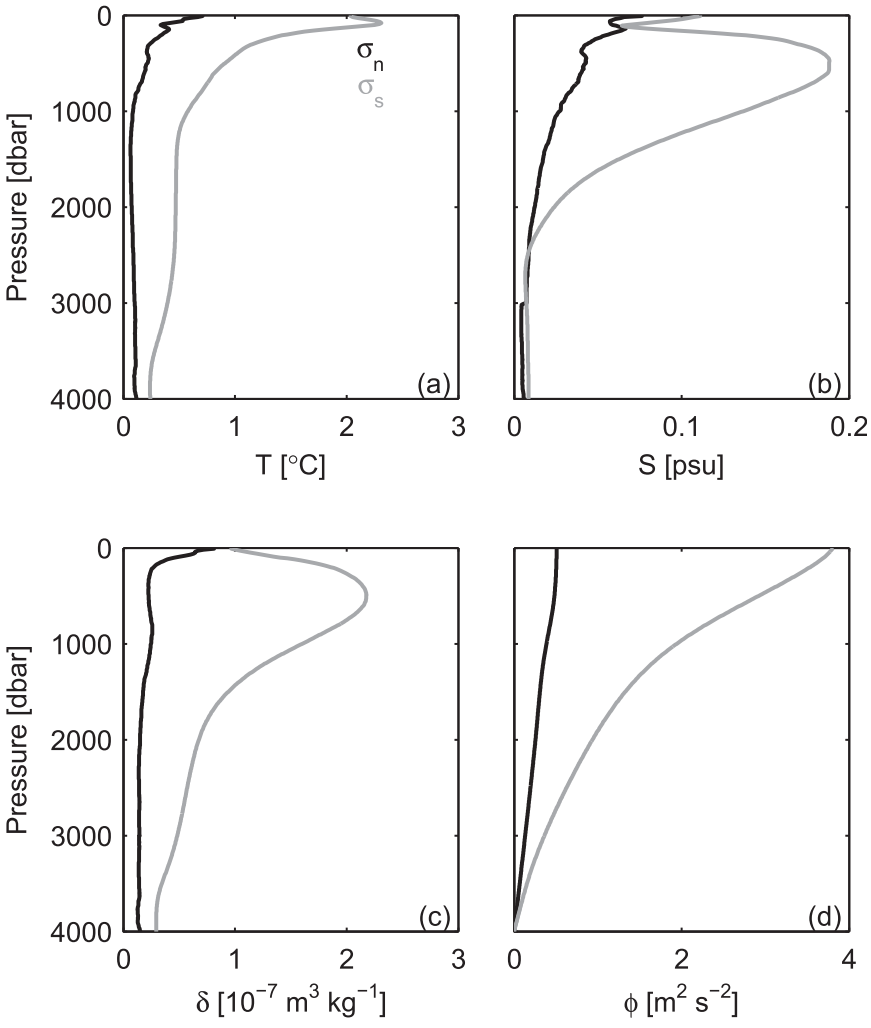

FIG. A4. Comparison of the std dev of the signals σ_s (gray lines) captured by the GEM splines with those of the scatter σ_n (black lines) about them determined from the hydrocasts plotted as functions of depth. In general, the signals exceed the noise, except for salinity below 2000 m where the signal is weak and nearly uniform at each depth.

Comparisons of the signals captured by the GEMs, defined as the total variance of the GEMs spline curve (σ_s^2) to the scatter about the fitted splines (or noise) defined as the variance of the residuals from the GEMs (σ_n^2), are shown in Fig. A4. The fraction of variance explained by the GEMs, calculated as $\epsilon = 1 - (\sigma_n^2/\sigma_s^2)$, was discussed previously in section 2c. We note here that the signals exceed the noise levels everywhere except for S at the deeper levels, where the signals vary weakly (see Fig. A2k).

Together Figs. A2–A4 illustrate that the dominant ACC water properties are well represented by the cDrake GEM lookup tables. Combining the CPIES-measured τ with the GEM tables is a robust method for estimating the time-variable ACC baroclinic transport through Drake Passage.

REFERENCES

Aoki, S., 2002: Coherent sea level response to the Antarctic Oscillation. *Geophys. Res. Lett.,* **29,** 1950, doi:10.1029/2002GL015733.

Baker-Yeboah, S., D. R. Watts, and D. A. Byrne, 2009: Measurements of sea surface height variability in the eastern South Atlantic from pressure sensor equipped inverted echo sounders: Baroclinic and barotropic components. *J. Atmos. Oceanic Technol.,* **26,** 2593–2609, doi:10.1175/2009JTECHO659.1.

Behnisch, M., A. Macrander, O. Boebel, J.-O. Wolff, and J. Schröter, 2013: Barotropic and deep-referenced baroclinic SSH variability derived from pressure inverted echo sounders (PIES) south of Africa. *J. Geophys. Res.,* **118,** 3046–3058, doi:10.1002/jgrc.20195.

Bindoff, N. L., and C. Wunsch, 1992: Comparison of synoptic and climatologically mapped sections in the South Pacific Ocean. *J. Climate,* **5,** 631–645, doi:10.1175/1520-0442(1992)005<0631:COSACM>2.0.CO;2.

Böning, C. W., A. Dispert, M. Visbeck, S. R. Rintoul, and F. U. Schwazkopf, 2008: The response of the Antarctic Circumpolar Current to recent climate change. *Nat. Geosci.,* **1,** 864–869, doi:10.1038/ngeo362.

Chereskin, T. K., K. A. Donohue, D. R. Watts, K. L. Tracey, Y. L. Firing, and A. L. Cutting, 2009: Strong bottom currents and cyclogenesis in Drake Passage. *Geophys. Res. Lett.,* **36,** L23602, doi:10.1029/2009GL040940.

——, ——, and ——, 2012: cDrake: Dynamics and transport of the Antarctic Circumpolar Current in Drake Passage. *Oceanography,* **25** (3), 134–135, doi:10.5670/oceanog.2012.86.

Cunningham, S. A., and M. Pavic, 2007: Surface geostrophic currents across the Antarctic Circumpolar Current in Drake Passage from 1992 to 2004. *Prog. Oceanogr.,* **73,** 296–310, doi:10.1016/j.pocean.2006.07.010.

——, S. G. Alderson, and B. A. King, 2003: Transport and variability of the Antarctic Circumpolar Current in Drake Passage. *J. Geophys. Res.,* **108,** 8084, doi:10.1029/2001JC001147.

Cutting, A. L., 2010: Constituents of sea surface height variability in Drake Passage. M.S. thesis, Department of Physical Oceanography, University of Rhode Island, 68 pp.

Donohue, K. A., D. R. Watts, K. L. Tracey, A. D. Greene, and M. Kenelly, 2010: Mapping circulation in the Kuroshio Extension with an array of current and pressure recording inverted echo sounders. *J. Atmos. Oceanic Technol.,* **27,** 507–527, doi:10.1175/2009JTECHO686.1.

Ferrari, R., C. Provost, A. Renault, N. Sennéchael, N. Barré, Y.-H. Park, and J. H. Lee, 2012: Circulation in Drake Passage revisited using new current time series and satellite altimetry: 1. The Yaghan Basin. *J. Geophys. Res.,* **117,** C12024, doi:10.1029/2012JC008264.

Firing, Y. L., T. K. Chereskin, and M. R. Mazloff, 2011: Vertical structure and transport of the Antarctic Circumpolar Current in Drake Passage from direct velocity observations. *J. Geophys. Res.,* **116,** C08015, doi:10.1029/2011JC006999.

——, ——, D. R. Watts, K. L. Tracey, and C. Provost, 2014: Computation of geostrophic streamfunction, its derivatives, and error estimates from an array of CPIES in Drake Passage. *J. Atmos. Oceanic Technol.,* **31,** 656–680, doi:10.1175/JTECH-D-13-00142.1.

Gille, S. T., and C. W. Hughes, 2001: Aliasing of high-frequency variability by altimetry: Evaluation from bottom pressure recorders. *Geophys. Res. Lett.,* **28,** 1755–1758, doi:10.1029/2000GL012244.

Griesel, A., M. R. Mazloff, and S. T. Gille, 2012: Mean dynamic topography in the Southern Ocean: Evaluating Antarctic Circumpolar Current transport. *J. Geophys. Res.,* **117,** C01020, doi:10.1029/2011JC007573.

Jackett, D. R., and T. J. McDougall, 1997: A neutral density variable for the world's oceans. *J. Phys. Oceanogr.,* **27,** 237–263, doi:10.1175/1520-0485(1997)027<0237:ANDVFT>2.0.CO;2.

Koshlyakov, M. N., I. I. Lisina, E. G. Morozov, and R. Y. Tarakanov, 2007: Absolute geostrophic currents in the Drake Passage based on observations in 2003 and 2005. *Oceanology,* **47,** 451–563, doi:10.1134/S0001437007040029.

Meijers, A. J. S., N. L. Bindoff, and S. R. Rintoul, 2011a: Estimating the four-dimensional structure of the Southern Ocean using satellite altimetry. *J. Atmos. Oceanic Technol.,* **28,** 548–568, doi:10.1175/2010JTECHO790.1.

——, ——, and ——, 2011b: Frontal movements and property fluxes: Contributions to heat and freshwater trends in the Southern Ocean. *J. Geophys. Res.,* **116,** C08024, doi:10.1029/2010JC006832.

Meinen, C. S., and D. R. Watts, 2000: Vertical structure and transport on a transect across the North Atlantic Current near 42°: Time series and mean. *J. Geophys. Res.,* **105,** 21 869–21 891, doi:10.1029/2000JC900097.

Meredith, M. P., and C. W. Hughes, 2005: On the sampling timescale required to reliably monitor interannual variability in the Antarctic circumpolar transport. *Geophys. Res. Lett.,* **32,** L03609, doi:10.1029/2004GL022086.

——, P. L. Woodworth, C. W. Hughes, and V. Stepanov, 2004: Changes in the ocean transport through Drake Passage during the 1980s and 1990s, forced by changes in the Southern Annular Mode. *Geophys. Res. Lett.,* **31,** L21305, doi:10.1029/2004GL021169.

——, and Coauthors, 2011: Sustained monitoring of the Southern Ocean at Drake Passage: Past achievements and future priorities. *Rev. Geophys.,* **49,** RG4005, doi:10.1029/2010RG000348.

Munk, W., and D. Cartwright, 1966: Tidal spectroscopy and prediction. *Philos. Trans. Roy. Soc. London,* **259,** 533–581, doi:10.1098/rsta.1966.0024.

Naveira Garabato, A. C., D. P. Stevens, and K. J. Heywood, 2003: Water mass conversion, fluxes, and mixing in the Scotia Sea diagnosed by an inverse model. *J. Phys. Oceanogr.,* **33,** 2565–2587, doi:10.1175/1520-0485(2003)033<2565:WMCFAM>2.0.CO;2.

Nowlin, W. D. J., T. Whitworth, and R. D. Pillsbury, 1977: Structure and transport of the Antarctic Circumpolar Current. *J. Phys. Oceanogr.,* **7,** 788–802, doi:10.1175/1520-0485(1977)007<0788:SATOTA>2.0.CO;2.

Olbers, D., and K. Lettmann, 2007: Barotropic and baroclinic processes in the transport variability of the Antarctic Circumpolar Current. *Ocean Dyn.,* **57,** 559–578, doi:10.1007/s10236-007-0126-1.

Orsi, A. H., T. Whitworth, and W. D. Nowlin Jr., 1995: On the meridional extent and fronts of the Antarctic Circumpolar Current. *Deep-Sea Res. I,* **42,** 641–673, doi:10.1016/0967-0637(95)00021-W.

Renault, A., C. Provost, N. Sennéchael, N. Barré, and A. Kartavtseff, 2011: Two full-depth velocity sections in the Drake Passage in 2006—Transport estimates. *Deep-Sea Res. II,* **58,** 2572–2591, doi:10.1016/j.dsr2.2011.01.004.

Rintoul, S. R., and Coauthors, 2010: Southern Ocean Observing System (SOOS): Rationale and strategy for sustained observations of the Southern Ocean. *Proceedings of OceanObs 09: Sustained Ocean Observations and Information for Society,* Vol. 2, J. Hall, D. E. Harrison, and D. Stammer, Eds., European Space Agency Publ. WPP-306, doi:10.5270/OceanObs09.cwp.74.

Smith, W. H. F., and D. T. Sandwell, 1997: Global sea floor topography from satellite altimetry and ship depth soundings. *Science,* **277,** 1957–1962, doi:10.1126/science.277.5334.1956.

Sokolov, S., and S. R. Rintoul, 2007: Multiple jets of the Antarctic Circumpolar Current south of Australia. *J. Phys. Oceanogr.,* **37,** 1394–1412, doi:10.1175/JPO3111.1.

——, and ——, 2009a: Circumpolar structure and distribution of the Antarctic Circumpolar Current fronts: 1. Mean circumpolar paths. *J. Geophys. Res.,* **114,** C11018, doi:10.1029/2008JC005108.

——, and ——, 2009b: Circumpolar structure and distribution of the Antarctic Circumpolar Current fronts: 2. Variability and

relationship to sea surface height. *J. Geophys. Res.,* **114,** C11019, doi:10.1029/2008JC005248.

Speer, K., S. R. Rintoul, and B. M. Sloyan, 2000: The diabatic Deacon cell. *J. Phys. Oceanogr.,* **30,** 3212–3222, doi:10.1175/1520-0485(2000)030<3212:TDDC>2.0.CO;2.

Sprintall, J., 2003: Seasonal to interannual upper-ocean variability in the Drake Passage. *J. Mar. Res.,* **61,** 27–57, doi:10.1357/002224003321586408.

Sun, C., and D. R. Watts, 2001: A circumpolar gravest empirical mode for the Southern Ocean hydrography. *J. Geophys. Res.,* **106,** 2833–2855, doi:10.1029/2000JC900112.

Swart, S., S. Speich, I. Ansorge, and R. Lutjeharms, 2010: An altimetry-based gravest empirical mode south of Africa: 1. Development and validation. *J. Geophys. Res.,* **115,** C03002, doi:10.1029/2009JC005299.

Thompson, D. J., and S. Solomon, 2002: Interpretation of recent Southern Hemisphere climate change. *Science,* **296,** 895–899, doi:10.1126/science.1069270.

Tracey, K. L., K. A. Donohue, D. R. Watts, and T. Chereskin, 2013: cDrake CPIES data report November 2007 to December 2011. Graduate School of Oceanography, University of Rhode Island GSO Tech. Rep. 2008-2, 72 pp. [Available online at http://digitalcommons.uri.edu/physical_oceanography_techrpts/4.]

Watts, D. R., C. Sun, and S. Rintoul, 2001: A two-dimensional gravest empirical mode determined from hydrographic observations in the Subantarctic Front. *J. Phys. Oceanogr.,* **31,** 2186–2209, doi:10.1175/1520-0485(2001)031<2186:ATDGEM>2.0.CO;2.

Whitworth, T., III, 1983: Monitoring the transport of the Antarctic Circumpolar Current at Drake Passage. *J. Phys. Oceanogr.,* **13,** 2045–2057, doi:10.1175/1520-0485(1983)013<2045:MTTOTA>2.0.CO;2.

——, and R. G. Peterson, 1985: Volume transport of the Antarctic Circumpolar Current from bottom pressure measurements. *J. Phys. Oceanogr.,* **15,** 810–816, doi:10.1175/1520-0485(1985)015<0810:VTOTAC>2.0.CO;2.